Spring 5-15-2023

Advancements in Magnetic Resonance Image Guided Radiotherapy

Austen Curcuru
Washington University in St. Louis

Recommended Citation

Curcuru, Austen, "Advancements in Magnetic Resonance Image Guided Radiotherapy" (2023). *McKelvey School of Engineering Theses & Dissertations*. 868.
https://openscholarship.wustl.edu/eng_etds/868

WASHINGTON UNIVERSITY IN ST. LOUIS

McKelvey School of Engineering
Department of Biomedical Engineering

Dissertation Examination Committee:
H Michael Gach, Chair
Hongyu An
Geoffrey Hugo
Abhinav Jha
Umberto Villa
Deshan Yang

Advancements in Magnetic Resonance Image Guided Radiotherapy

by
Austen Curcuru

A dissertation presented to

the McKelvey School of Engineering

of Washington University in

partial fulfillment of the

requirements for the degree

of Doctor of Philosophy

August 2023

St. Louis, Missouri

Table of Contents

List of Figures

List of Tables

Acknowledgements

This research was funded under National Institutes of Health (NIH) National Heart, Lung, and Blood Institute (NHLBI) grant R01 HL148210. This research was conducted under a Master Research Agreement (MRA) between Washington University in St. Louis and ViewRay.

I want to thank David Holloway and Rajiv Lotey of ViewRay, Washington University School of Medicine physicists Olga Green, Tom Mazur, Taeho Kim, and Robert Morris, and my entire Dissertation Committee for their assistance and advice. Additionally, I would like to offer thanks to my advisor, H Michael Gach, for his invaluable insight, support, and encouragement.

Finally, I want to thank all of my family and friends that had to listen to me explain what a B_0 eddy current is.

Austen Curcuru

Washington University in St. Louis

August 2023

Dedicated to my wife, Laura Curcuru

ABSTRACT OF THE DISSERTATION

Advancements in Magnetic Resonance Image Guided Radiotherapy

by

Austen Curcuru

Doctor of Philosophy in Biomedical Engineering

Washington University in St. Louis, 2023

Professor H. Michael Gach, Chair

Magnetic resonance image guided radiation therapy (MRgRT) devices are a recently developed technology that integrate the excellent soft tissue contrast and real-time imaging capabilities of MRI with a medical linear accelerator (Linac). This provides an unprecedented ability to guide and adapt radiation therapy treatments based on real-time cine imaging. However, the merging of these technologies has come with unique challenges.

MRI lacks the geometric fidelity of computed tomography (CT). Spatial inaccuracies in MRI can result from magnetic field (B_0) or center frequency variations, gradient-induced eddy currents, and magnetic field gradient imperfections (e.g., nonlinearities, poor calibration, concomitant fields, and unsatisfactory electronic fidelity). Previous work identified gantry angle dependent shifts in the imaging isocenter of a commercial 0.35 T MRI-Linac.

Additionally, the balanced steady state free precession (bSSFP) sequences used in MRgRT offer excellent signal to noise ratios (SNRs) and temporal resolution, but require high levels of B_0 homogeneity, B_0 stability, and precise control over the gradient systems. Banding artifacts appear in the resulting images if these stipulations are violated and intravoxel dephasing approaches an odd multiple of π. Rotation of the radiation therapy gantry also results electromagnetic interference (EMI). The gantry-related EMI causes banding artifacts on images collected during that time.

Similarly, cardiac implanted electronic devices (CIEDs) result in magnetic susceptibility artifacts primarily due to ferromagnetic components. These artifacts manifest as banding artifacts in bSSFP images and make tracking structures in or near the heart challenging during treatment imaging.

The work presented in this dissertation investigates and quantifies the causes of imaging isocenter shifts, develops a method for real-time B_0 compensation during rotation of the radiation therapy gantry, and introduces a deep learning solution to CIED induced artifacts on a commercial low-field MRgRT system.

Chapter 1: Introduction and Overview

“If you can’t see it, you can’t hit it, and if you can’t hit it, you can’t cure it.”

-Dr. Harold Johns, Medical Physicist

Cancer is the second leading cause of death behind heart disease with an estimated 1,900,000 new cases and 600,000 deaths in the USA in 2022.[1] National Cancer Institute statistics estimate 60% of people with cancer will undergo radiotherapy.[2] Most radiotherapy treatment in the USA is performed on a linear accelerator (Linac). The megavolt photon beam of the Linac deposits dose to the tumor leading to cell death. However, ionizing radiation is harmful to healthy tissues as well. The overarching goal of radiotherapy is therefore to deliver enough dose to the kill tumor while sparing nearby critical structures.[3] Technological advancements are designed to improve the dose conformality, reduce treatment uncertainties, and spare healthy tissue in radiotherapy.

The introduction of computed tomography (CT) and 3D dose optimization algorithms resulted in dramatic improvements in radiotherapy planning.[4] Patients receive a planning CT (i.e., CT simulation) prior to treatment. A team consisting of medical physicists, radiation oncologists, and dosimetrists then generate and approve a radiotherapy plan using the simulation CT. The gross tumor volume (GTV) is identified on the images and margins around it are expanded to deal with uncertainties in patient setup, physiological motion, minor changes to the patient anatomy, the accuracy of the treatment delivery, and microscopic diseased tissue that cannot be directly localized on the image. Organs at risk (OARs) are additionally contoured to ensure that the dose received by those structures remains below thresholds known to cause radiotoxicity. The initial radiotherapy plan is therefore based on the patient anatomy on the day of the CT simulation. Patient motion and peristalsis during treatment (intrafactional movement) and changes to the underlying patient anatomy between treatments (interfractional motion) can result in suboptimal treatment if not properly accounted.[5,6]

As cone-beam CT (CBCT) imaging functionalities became standard equipment on medical linear accelerators, patient alignment uncertainties were further reduced.[7] Patients could receive a CBCT immediately prior to radiotherapy treatment and the images could be aligned with the planning CT to ensure consistent positioning. However, CBCT results in poor soft tissue contrast, relatively low image quality, and additional ionizing radiation across the imaging volume. Additionally, CBCT images are acquired for patient setup but are not continuously acquired throughout treatment.[8] Fluoroscopy can be utilized treatment but the additional ionizing radiation limits how the real-time imaging duty cycle

1.1 Magnetic Resonance Image Guided Radiotherapy

Magnetic resonance imaging (MRI) offers several advantages over other medical imaging modalities. MRI offers exceptional soft tissue contrast without imparting any ionizing radiation which makes it a valuable modality for radiotherapy.[9–12] High resolution 3D setup MRIs can be used in place of a CBCT to ensure proper patient alignment. Additionally, MRI guided radiotherapy (MRgRT) systems provide real-time target tracking that can be performed continuously throughout treatment. This allows for treatment gating, or halting the beam when the target is outside of the prescribed radiotherapy field, without relying on a motion surrogate.[10] Motion surrogates may become decorrelated with tumor motion during treatment resulting in suboptimal radiation delivery whereas gating on an MRgRT system allows for direct localization of the tumor.[13,14]

MRgRT facilitates online adaptive radiotherapy. Images acquired on an MRgRT system are better able to visualize the lesion and the surrounding organs at risk versus CBCT systems.[8] The radiotherapy plan can be adjusted prior to the delivery of each fraction and while the patient is on the radiotherapy table to ensure that OAR constraints are met and/or allow for the safe escalation of dose to the treatment target. Stereotactic MRI-guided online adaptive radiation therapy (SMART) protocols have resulted in substantial increases in two-year overall survival in patients with inoperable pancreatic cancers.[15,16]

MRgRT still comes with several technical hurdles. MRI lacks the geometric fidelity of CT. Changes to the primary magnetic field (B_0), eddy currents caused by gradient switching, and gradient field imperfections can lead to spatial inaccuracies and geometric distortion. Stereotactic radiosurgery (SRS), a form of radiotherapy where high doses are focused on a small area over a shorter fractionation schedule, requires spatial accuracies of ≤1 mm.[17]Traditional intensity modulated radiation therapy (IMRT) requires spatial accuracies of ≤2 mm.[17] Previous studies reported shifts in the imaging isocenter of a 0.35 T ViewRay MRIdian MRI-Linac (ViewRay Inc., Mountain View, USA) based on the position of the radiotherapy gantry.[18] **Chapter 2** investigates the root causes of these imaging shifts and quantifies the effects of eddy currents as a function of the radiotherapy gantry position.

Commercial MRgRT systems are currently restricted to step-and-shoot IMRT. This means that the radiotherapy gantry and multi-leaf collimators (MLCs) are stationary while the beam is on.[9–11] Volumetric modulated arc therapy (VMAT) is a delivery technique where the beam remains on while the gantry and MLCs are moving. VMAT can improve patient throughput and improve dose conformality compared with step-and-shoot IMRT.[19–21] Gantry rotation on ViewRay's MRI-Linac currently results in imaging artifacts that would be unacceptable for VMAT treatment.[18,22] **Chapter 3** implements a custom pulse sequence on the MRI subsystem of a 0.35 T MRIdian MR-Linac that compensates for B_0 fluctuations caused by gantry rotation in real time to reduce imaging artifacts.

MRgRT shows significant potential in improving cardiac radioablation (CRA). CRA is a noninvasive procedure pioneered at Washington University in Saint Louis to treat ventricular tachycardia (VT) refractory to standard drug and catheter ablation therapy.[23,24] CRA is typically performed using cone beam CT image guided radiation therapy (CBCT-IGRT to deliver 25 Gy in a single fraction to the myocardial lesion that produces the arrythmia. Currently, the treatment target needs to be expanded by 7-10 mm to account for motion, gating uncertainties inherent to CBCT-IGRT, and patient setup.[24] These margin expansions result in healthy tissue receiving therapeutic radiation doses. Because MRgRT enables continuous imaging during treatment and beam gating without relying on a motion surrogate, radiotoxicities and target margins could potentially be reduced by adopting an MRgRT approach to CRA. Unfortunately, the magnetic susceptibility of implanted cardiac devices common in patients suffering from VT results in null-band artifacts in balanced steady-state free precession (bSSFP) cine

MRIs typically used in MRgRT. Cines acquired using other traditional pulse sequences that are less susceptible to artifacts than bSSFP sequences0.35 T sacrifice SNR, temporal resolution, spatial resolution, or contrast-to-noise ratio (CNR). **Chapter 4** investigates using deep learning to reduce cardiac internal electronic device (CIED) artifacts in bSSFP cine images.

Chapter 2: Quantifying the Effects of B_0 eddy currents on imaging isocenter shifts in a 0.35 T MRI-Linac

This chapter has been published in the journal Medical Physics, 2021 Jun;48(6):2929-2938. doi: 10.1002/mp.14842. Text, figures, equations, and references have been modified from the published work for consistency with the thesis.

2.1 Introduction

MRgRT systems offer real-time tumor tracking and excellent soft tissue contrast without the use of additional ionizing radiation for image guidance.[9–12] However, MRI lacks the geometric fidelity of CT. Spatial inaccuracies in MRI can result from magnetic field (B_0) or center frequency variations, gradient-induced eddy currents, and magnetic field gradient imperfections (e.g., nonlinearities, poor calibration, concomitant fields, and unsatisfactory electronic fidelity).[25,26]

Gantry angle-dependent shifts in the imaging isocenter were reported on a 0.35 T MRI-Linac system. A maximum displacement of 1.8 mm for 3D true fast imaging with balanced steady-state precession (TrueFISP) scans used for treatment planning and patient setup was measured.[18] A maximum displacement of 0.9 mm for 2D cine TrueFISP used in real-time treatment delivery and beam gating was also observed.[18] Stereotactic radiosurgery (SRS) requires a spatial accuracy of ≤1 mm while radiation therapy requires a nominal spatial accuracy of ≤2mm.[17]

Previous studies quantified B_0 inhomogeneities (ΔB) and gradient nonlinearities in commercial MRI-Linac systems.[27–30] For the 0.35 T MRI-Linac, the measured quantities of ΔB and gradient nonlinearities were too small to explain the magnitude of the observed imaging isocenter shifts. Therefore, alternative causes of the imaging isocenter shifts were sought.

MRgRT systems use rotating gantries that can cause gantry angle-dependent variations in eddy currents.[31] Gradient (first order) eddy currents cause k-space trajectory errors that can result in image distortion (e.g., translation, shearing, and scaling) and artifacts.[32,33] Localized shifts resulting from gradient eddy currents will be spatially variant. Thus, imaging isocenter shifts for such an object are most likely caused by center frequency offsets or B_0 eddy currents during image acquisition.

The purpose of this study was to quantify eddy currents in a commercial 0.35 T MRI-Linac and test the hypothesis that B_0 eddy currents are the primary cause of imaging isocenter shifts. To date, there have been no studies that quantified eddy currents in MR-IGRT systems as a function of gantry angle. Eddy currents are typically measured and compensated at a single gantry angle during system commissioning or after significant servicing.

2.2 Material and Methods

2.2.1 Theory

For a 2D Cartesian acquisition, the acquired signal for the nth phase encode line of k-space can be modeled as:[34]

$$s_n(t;\tau_{PE}) = \iint \rho(r_{RO}, r_{PE}) \exp[-i\Delta\omega t] \left(\exp\left[-i\int_0^{\tau_{PE}} \gamma G_{PE,n}(t')(r_{PE} + b_{PE})dt'\right]\right)\left(\exp\left[-i\int_0^{\tau_{PE}} \gamma G_{RO}(t'')(r_{RO} + b_{RO})dt''\right]\right) dr_{RO}dr_{PE} \qquad (2.1)$$

where ρ is the spin density, r_{RO} and r_{PE} are the spatial coordinates for the readout (RO) and phase encode (PE) axes, G_{RO} is the readout gradient amplitude, $G_{PE,n}$ is the nth phase encode gradient amplitude, Δω represents field inhomogeneity or center frequency offsets, b_{RO} and b_{PE} are the B_0 (zeroth order) eddy current factors (in units of length), τ_{PE} is the phase encode duration, and γ is the gyromagnetic ratio. Gradient (first order) eddy currents are incorporated as fractional errors in G_{PE} and G_{RO}. This model ignores moving spins, T_1 and T_2 relaxation, and the various causes of signal attenuation (e.g., coil sensitivity and filling factor). The model also ignores residual eddy currents from concurrent or prior gradient ramps, for example, residual eddy currents from the slice-selective gradient during the phase encode, or residual eddy currents from the phase encode gradient(s) during the readout. Eq. (2.1) can be rewritten as:

$$s_n(t;\tau_{PE}) = \iint \rho(r_{RO}, r_{PE}) \exp[-i\Delta\omega t] \left(\exp\left[-i\left[\gamma \tilde{G}_{PE,n}\left(r_{PE} + \tilde{b}_{PE}\right)\right]\tau_{PE}\right]\right)\left(\exp\left[-i\int_0^{\tau_{PE}} \gamma G_{RO}(t'')(r_{RO} + b_{RO})dt''\right]\right) dr_{RO}dr_{PE} \qquad (2.2)$$

where $\tilde{b}_{PE}$ and $\tilde{G}_{PE,n}$ are b_{PE} and $G_{PE,n}$ averaged over the phase encode duration, respectively. The model can be extended to 3D using a second (slice) phase encode.

A shift of $\Delta\omega/(\gamma G_{RO})$ occurs in the readout direction in the image domain. A B_0 eddy current from a phase encode gradient causes a shift of $\tilde{b}_{PE}$ along r_{PE} in the image domain and signal dephasing during readout.[35] A B_0 eddy current from a readout gradient causes a shift of approximately $b_{RO}(TE)$ along r_{RO} in the image domain, where TE is the echo time. Residual B_0 eddy currents from additional phase encode axes (e.g., slice phase encode for 3D acquisitions) introduce a phase in the readout signal that varies with k-space line resulting in signal dephasing in the image domain. Residual B_0 eddy currents from the slice-selective gradient rephaser will be consistent between k-space lines contributing to the isocenter shift during readout. B_0 eddy currents during non-Cartesian acquisitions can cause signal dephasing and image nonuniformity.[36,37]

2.2.2 Measurements

Experiments were conducted on a 0.35 T MRI-Linac (ViewRay, Oakwood Village, OH) before and after upgrade from version 2.0 to 2.0.2. The Linac's radiofrequency (RF) waveguide was replaced during the upgrade to move it further away from the MRI components and reduce imaging isocenter shifts (Fig. 2.1).

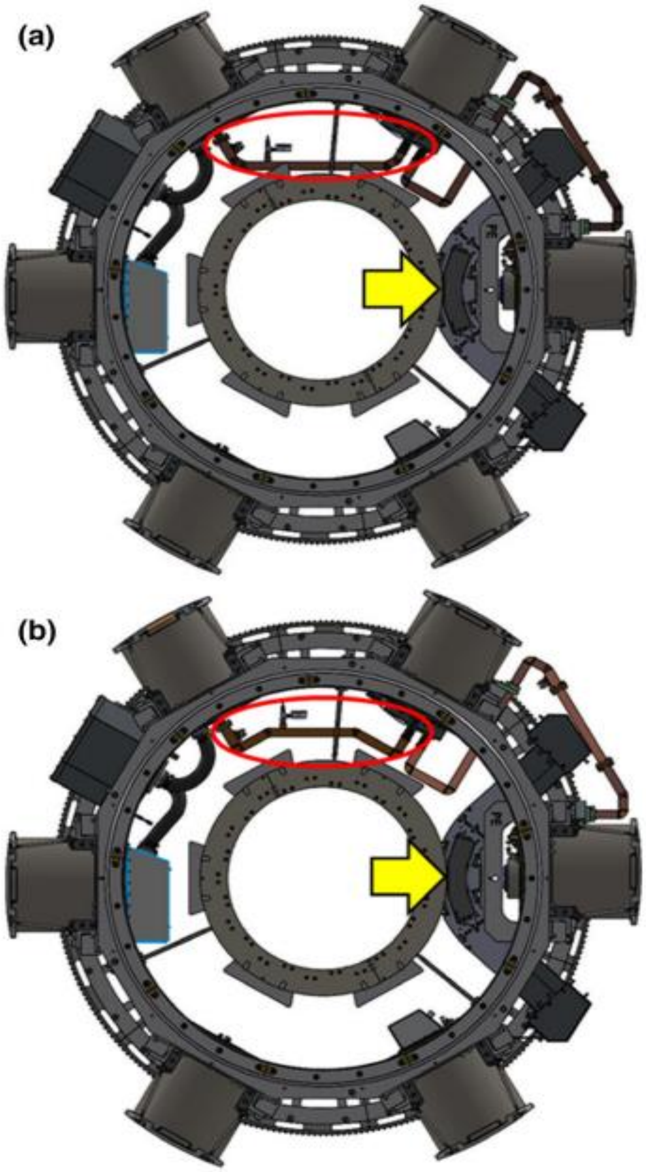

Figure 2.1: Configuration of the ViewRay MRI-Linac gantry before (a) and after (b) the 2020 system V2.0.2 upgrade. Note the waveguide (circled in red) was closer to the center of the bore and gradient coils before the upgrade. The Linac and multileaf collimators are indicated by the arrow. Images courtesy of ViewRay

The MRI subsystem electronics were based on the Siemens Avanto MRI system and ran Siemens IDEA/ICE software VB19. Eddy currents and field homogeneity were measured and adjusted to meet system specifications by ViewRay engineers at gantry angle 0° using Siemens' proprietary eddy current compensation (ECC) tool. The tool used a spin echo acquisition with variable delays and echo times to measure eddy current data from 0.39 to 9000 ms after the gradient pulse. The tool was used to calculate five time constants and amplitudes for each gradient axis, three B_0 time constants and amplitudes for each gradient axis, and one time constant for each of the six cross-term eddy currents. Iterations were performed until the eddy currents were within specifications (Table 2.1).

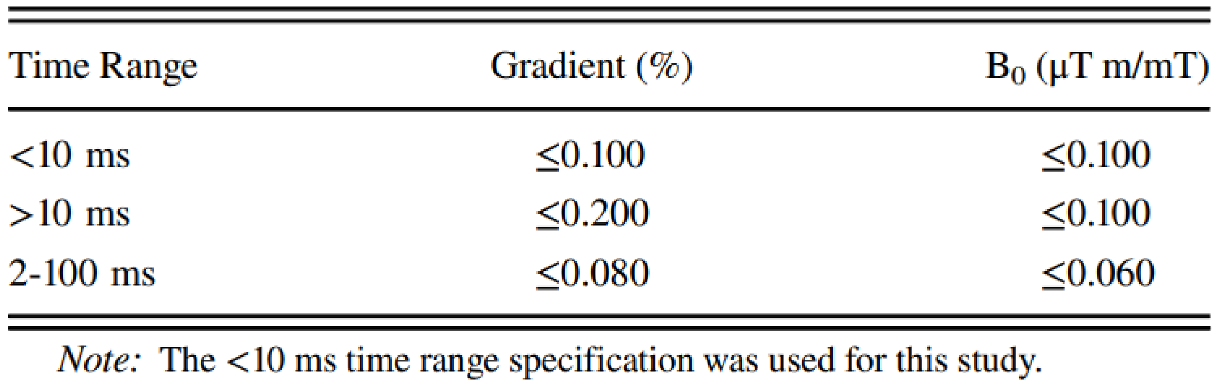

Time Range	Gradient (%)	B_0 (μT m/mT)
<10 ms	≤0.100	≤0.100
>10 ms	≤0.200	≤0.100
2-100 ms	≤0.080	≤0.060

Note: The <10 ms time range specification was used for this study.

TABLE 2.1: Siemens eddy current specifications for maximum magnitudes

The proprietary Siemens ECC tool requires service-level access. In addition, the tool uses a fixed, phantom-based shim ("Tune Up" shim mode) based on the field homogeneity at 0°. The measurement may fail from strong spin dephasing if used at gantry angles other than 0° since there are variations in field homogeneity with gantry angle and the tool does not reshim the magnetic field prior to the measurement of eddy currents.[30] The tool also requires and verifies phantom position offsets of ≤5 mm for X and Y axes, and ≤3 mm for the Z axis before acquiring eddy current measurements.

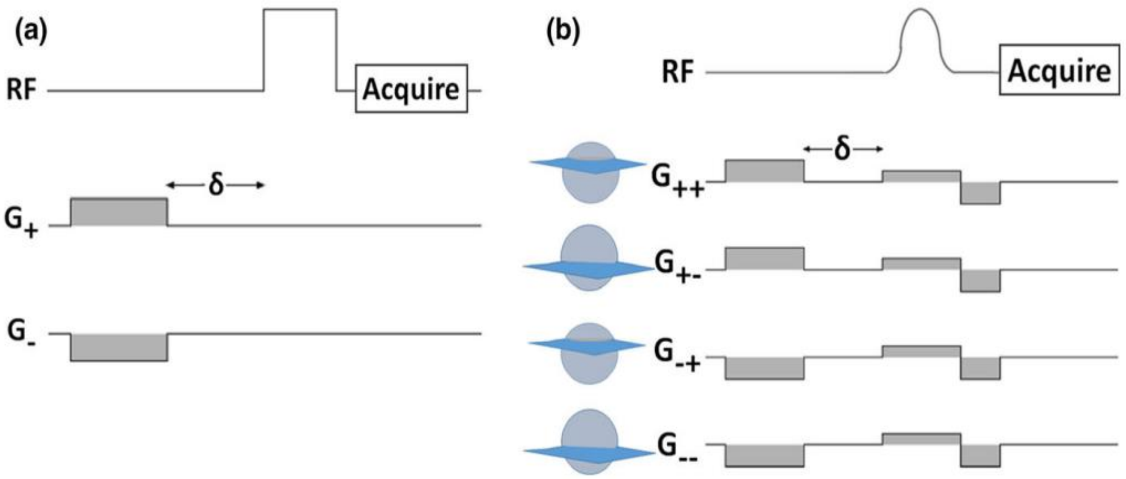

Figure 2.2: Nonselective (a) and slice-selective (b) pulse sequences used to measure eddy currents stimulated by the gradient (G). The first subscript represents the gradient pulse polarity. The second subscript represents the slice offset direction relative to the imaging isocenter. For both sequences, alternating polarity gradient pulses were placed before the RF excitation to stimulate the eddy currents. A variable delay (δ) was placed between the gradient pulse and the RF excitation. An FID was acquired to sample the eddy currents.

Therefore, we created two custom pulse sequences (Table 2.2) that allowed us to reshim at each gantry angle and characterize the gantry angle-dependent eddy currents. First, we measured B_0 eddy currents using a customized free induction decay (FID) sequence with a nonselective RF excitation. Second, we measured gradient and B_0 eddy currents using a slice-selective pulse sequence derived from a fast low angle shot (FLASH) sequence. Herein, these sequences are referred to as “nonselective” and “slice selective”, respectively.

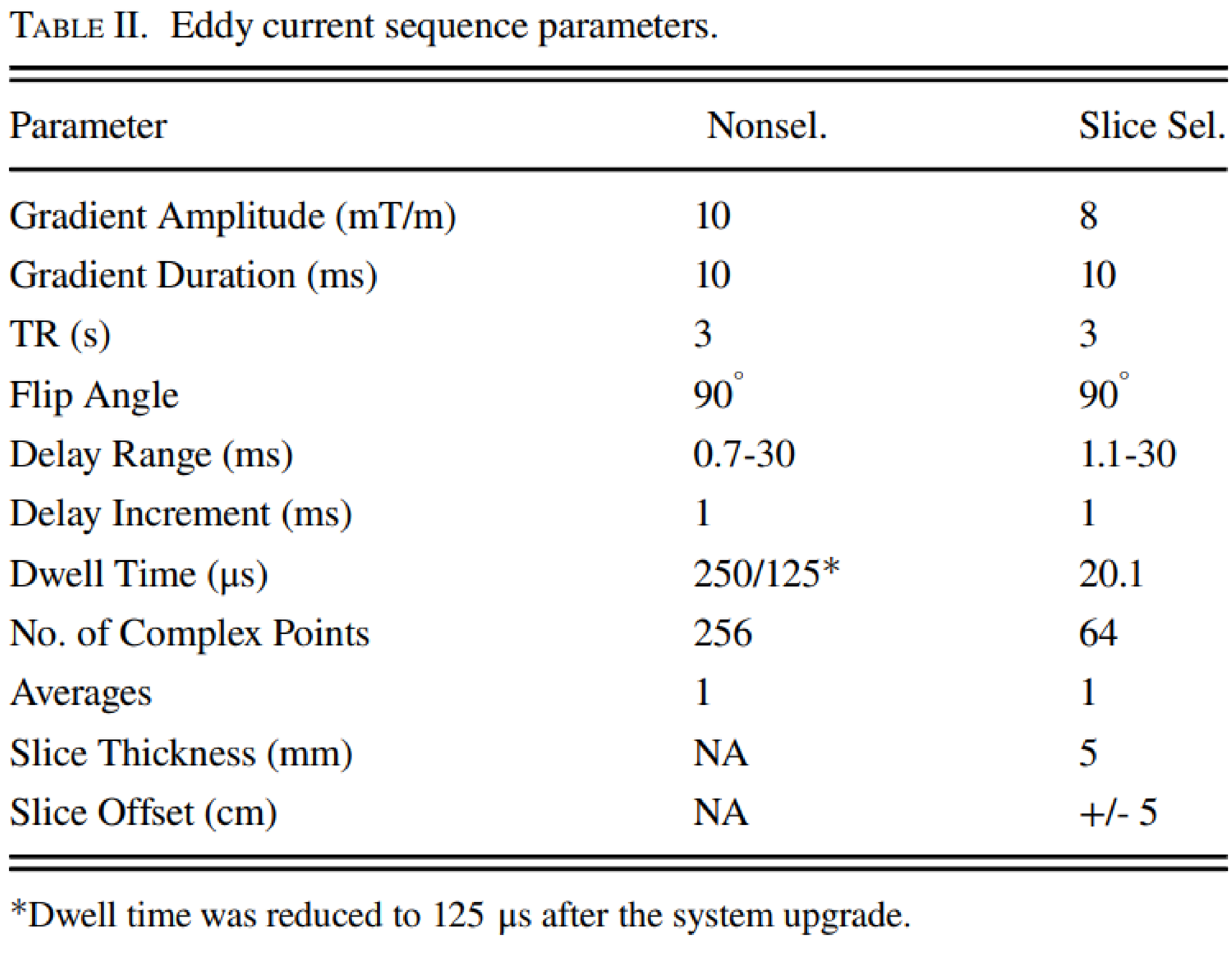

TABLE II. Eddy current sequence parameters.

Parameter	Nonsel.	Slice Sel.
Gradient Amplitude (mT/m)	10	8
Gradient Duration (ms)	10	10
TR (s)	3	3
Flip Angle	90°	90°
Delay Range (ms)	0.7-30	1.1-30
Delay Increment (ms)	1	1
Dwell Time (µs)	250/125*	20.1
No. of Complex Points	256	64
Averages	1	1
Slice Thickness (mm)	NA	5
Slice Offset (cm)	NA	+/- 5

*Dwell time was reduced to 125 µs after the system upgrade.

Table 2.2: Eddy current sequence parameters.

Measurements of eddy currents, field homogeneities, and center frequencies were performed using a spherical 24-cm DSV phantom doped with 5 mM $NiSO_4$ (T_1/T_2: 330/260 ms at 0.35 T) using the body RF coil for RF signal transmission and reception. Measurements were acquired in the MRI QA mode. The phantom was centered at the imaging isocenter using the external laser positioning system with the gantry angle set to 0°. The position was verified on the three-plane localizer images and corrected as required to keep isocenter offsets < 3mm.

Scans were acquired with the gantry positioned at every 30° ranging from 0° to 330°. The system was shimmed and tuned at each gantry angle prior to data acquisition. Measurements were repeated for each gradient axis (X, Y, Z). Herein, all measurements will be reported using Dicom coordinates with X axis (from right to left), Y axis (from anterior to posterior), and Z axis (from foot to head), and assuming a head first, supine patient position.

2.2.3 B_0 Eddy Currents

B_0 eddy currents were measured by pulsing the gradient and measuring its effect on an FID signal resulting from a nonselective (rectangular) RF pulse (Fig. 2.2). The sampling dwell time was reduced from 250 μs to 125 μs following the waveguide upgrade to capture additional detail in the B_0 eddy current curves. Gradient ramp up/down times were set at 150 μs. Following a reference scan without a gradient pulse, 31 pairs of FID measurements were acquired by incrementing the delay (δ) between the end of the gradient pulse and the beginning of the RF pulse from 0 ms to 30 ms in 1 ms increments. In addition to δ, a fixed delay of 500 μs was used to avoid measurements during the RF pulse. An additional delay of 100 μs was placed after the end of the RF pulse to protect the receiver from RF coil ring-down.[38]

Following phase unwrapping, the FID phase measured over the volume was:

$$\phi_{\pm}(t) = \pm\gamma\int_0^t B_0(\tau)d\tau + \Delta\omega t + \phi_0 \qquad (2.3)$$

where $B_0(\tau)$ represents the B_0 eddy current and ϕ_0 is the baseline phase. The static terms were removed by subtracting the phase acquired with the gradient polarity reversed:[34]

$$\phi(t) = \frac{\phi_+ - \phi_-}{2} = \gamma \int_0^t B_0(\tau)\, d\tau \quad (2.4)$$

where + and − represent the gradient polarities. The B_0 eddy current was calculated after time differentiation of ϕ. Phase unwrapping and subsequent analysis were performed using MATLAB (2019a, The MathWorks Inc). The resulting B_0 eddy current measurement (in units of μT) was normalized to the applied gradient amplitude (in units of mT/m) thus producing the normalized B_0 eddy current factor (presented in units of μT m/mT or mm) for comparison with the Siemens specification.

2.2.4 Gradient Eddy Currents

Gradient and B_0 eddy currents were measured simultaneously using a slice-selective sequence that combined measurements from two parallel slices, equidistant from isocenter, and gradient polarity cycling (Fig. 2.2). A variable delay (δ) was incremented from 0 ms to 30 ms in 1 ms increments after the gradient pulse to acquire overlapping data and to extend the effective measurement time. In addition to δ, a fixed delay of 1.1 ms was included between the gradient pulse and the start of the data acquisition to prevent acquisition during the selective RF excitation. Following phase unwrapping, FID signal phases derived from the four measurements were described by:[39]

$$\phi_{++}(t) = 2\pi k(t) r_0 + \phi_{B_0}(t) + \Delta\omega(r_0) t + \phi(r_0, t) \qquad (2.5)$$

$$\phi_{-+}(t) = -2\pi k(t) r_0 - \phi_{B_0}(t) + \Delta\omega(r_0)t + \phi(r_0, t) \quad (2.6)$$

$$\phi_{+-}(t) = -2\pi k(t) r_0 + \phi_{B_0}(t) + \Delta\omega(-r_0)t + \phi(-r_0, t) \quad (2.7)$$

$$\phi_{--}(t) = 2\pi k(t) r_0 - \phi_{B_0}(t) + \Delta\omega(-r_0)t + \phi(-r_0, t) \quad (2.8)$$

where the first subscript represents the gradient pulse polarity, the second subscript represents the slice offset ($\pm r_0$) polarity, k represents the k-space resulting from the gradient eddy current. The gradient eddy currents were calculated using:

$$2\pi k(t)_0 = \frac{1}{4}[(\phi_{++} - \phi_{-+}) - (\phi_{+-} - \phi_{--})] = \gamma \int_0^t G(\tau) r_0 \, d\tau \quad (2.9)$$

$$\phi_{B_0}(t) = \frac{1}{4}[(\phi_{++} - \phi_{-+}) + (\phi_{+-} - \phi_{--})] = \gamma \int_0^t B_0(\tau) d\tau \quad (2.10)$$

The eddy currents were obtained after time differentiation of $\phi_{B_0}$and k. The slice-selective eddy current data were smoothed with a 10-point moving average filter (MATLAB "smooth" function) prior to numeric differentiation to reduce noise variance. In one case (pre-upgrade Z axis eddy currents), additional filtering was applied because the data had an abnormally high noise baseline. The measured gradient eddy current was normalized to the applied gradient amplitude and presented in percent. For both the nonselective and slice-selective methods, eddy current data had redundant sample times since the acquisition time was larger than the delay times. Therefore, eddy current data acquired at different delay times were averaged together based on their sample time after the gradient pulse. For the slice-selective data, the different delay measurements were all interpolated to a common time base using linear interpolation prior to averaging.

The root mean square (RMS) was calculated for the peak B_0 and gradient eddy currents (delays < 10 ms) and the various gantry angles to assess the effects of the waveguide upgrade. A paired two-tailed t-test was performed to assess the significance of changes.

2.2.5 B_0 Inhomogeneity

B_0 inhomogeneities and center frequencies were measured at each gantry angle by acquiring conventional FIDs in the spherical phantom [repetition time (TR): 3 s, flip angle (FA): 90°, 4 Averages, receiver bandwidth (rBW): 1 Hz/pt for 1024 complex points]. FIDs were averaged and converted into a spectrum using a discrete fast Fourier transform (FFT). The resulting spectrum was fit to a Lorentzian function to obtain the full width at half maximum (FWHM) and center frequency (B_0).

2.2.6 Imaging Isocenter Shifts

Imaging isocenter shifts were measured using a 33 × 33 × 10.5 cm^3 Fluke 76-907 uniformity linearity water phantom doped with 15 mM $CuSO_4$ (HP Manufacturing, Cleveland, OH). At gantry angle 0°, the grid portion of the phantom was centered at the isocenter using the external laser positioning system and localizer to ensure isocenter offsets were acquired once with the phantom aligned along axial, coronal, and sagittal slice orientations (TR/echo time (TE): 3.37/1.44 ms, flip angle: 60°, rBW: 534 Hz/pixel, FOV: 350 × 350 × 108 mm^3, voxel size: 1.5 × 1.5 × 3 mm^3) using the body RF coil. The system was shimmed and tuned prior to each measurement at each gantry angle. Analysis software from ViewRay was used to calculate the in-plane isocenter shifts for each gradient axis from each phantom orientation and gantry angle relative to the centroid measured at gantry angle 0°.[18] The correlations between the isocenter shifts and the peak eddy currents (<10 ms) were calculated with and without the Z axis data.

The RMS was calculated for the imaging isocenter shifts at various gantry angles to assess the effects of the waveguide upgrade. A paired two-tailed t-test was performed to assess significance of the changes.

2.3 Results

2.3.1 B_0 Eddy Currents

An example of B_0 eddy currents measured using the nonselective vs slice-selective excitation is shown in Fig. 2.3. The eddy currents are typically highest at the shortest delay times.

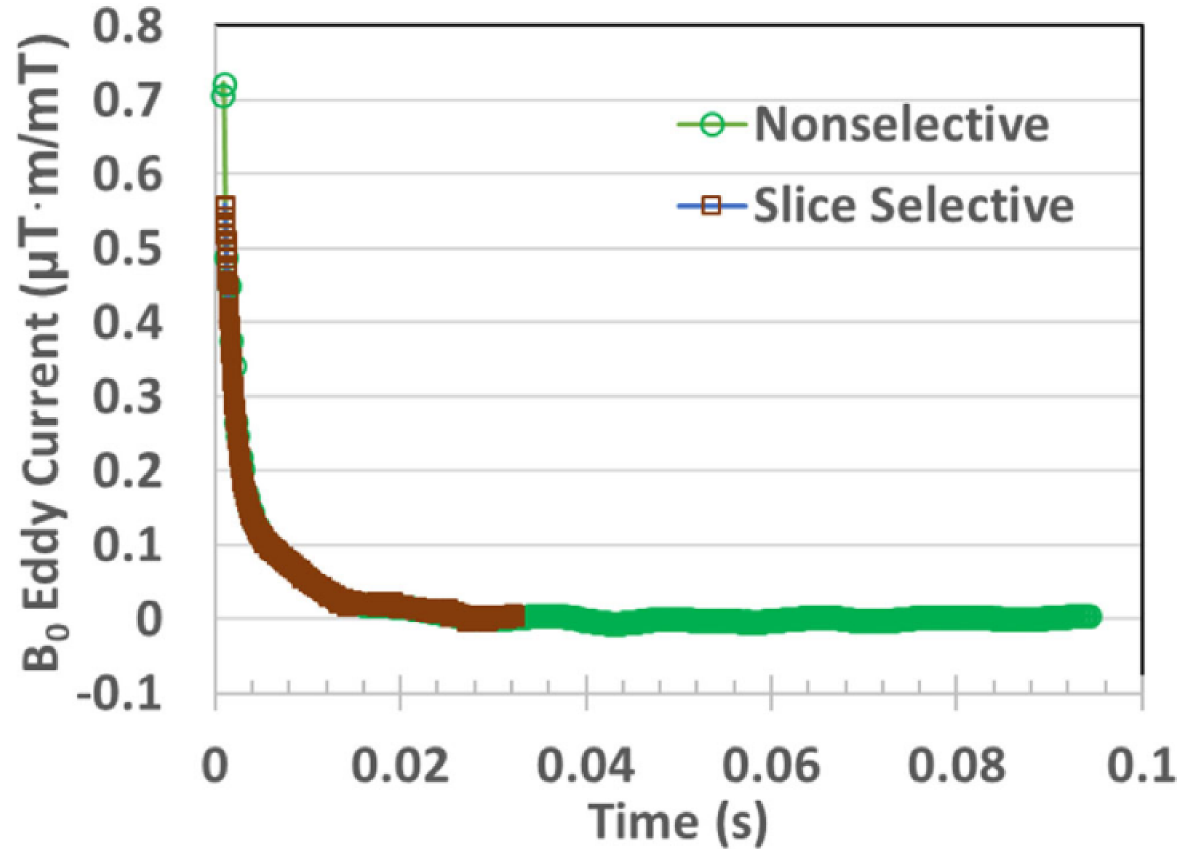

Figure 2.3: Example of comparison of B_0 eddy currents resulting from nonselective vs slice-selective acquisitions for X gradient pulse at gantry angle 150° acquired before the waveguide upgrade. Note there is good consistency between the methods. The nonselective data sampled shorter delays and covered a larger time range due to its long sampling dwell time.

The peak amplitudes of B_0 eddy currents (delays < 10 ms) measured with the nonselective sequence before and after the waveguide upgrade are shown in Fig. 2.4. The peak amplitudes of B_0 eddy currents measured with the slice-selective sequence are shown in the (Figure 2.5). Z gradients, both before and after the waveguide upgrade, produced smaller B_0 eddy currents compared to gradients played out along the X and Y axes.

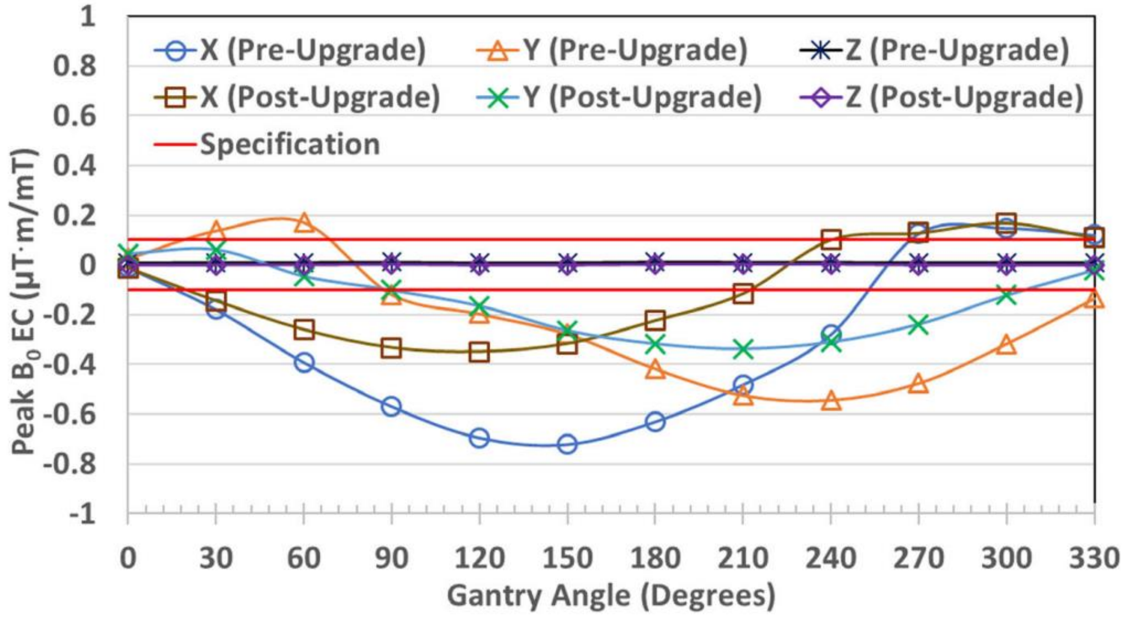

Figure 2.4: Comparison of peak amplitudes of B_0 eddy currents for delays <10 ms, measured before and after the Linac RF waveguide upgrade using the nonselective excitation. Most B_0 eddy currents associated with the X and Y gradients did not meet the vendor's specification (region between red lines).

Correlations between the B_0 eddy current results measured using the nonselective vs slice-selective method were high (0.986, $P \ll 0.001$). We used the nonselective B_0 eddy current measurements for the isocenter shift analyses due to their shorter delay times and lower noise. Root mean square peak B_0 eddy currents dropped 45.47% ($P < 0.002$) as a result of the Linac waveguide upgrade.

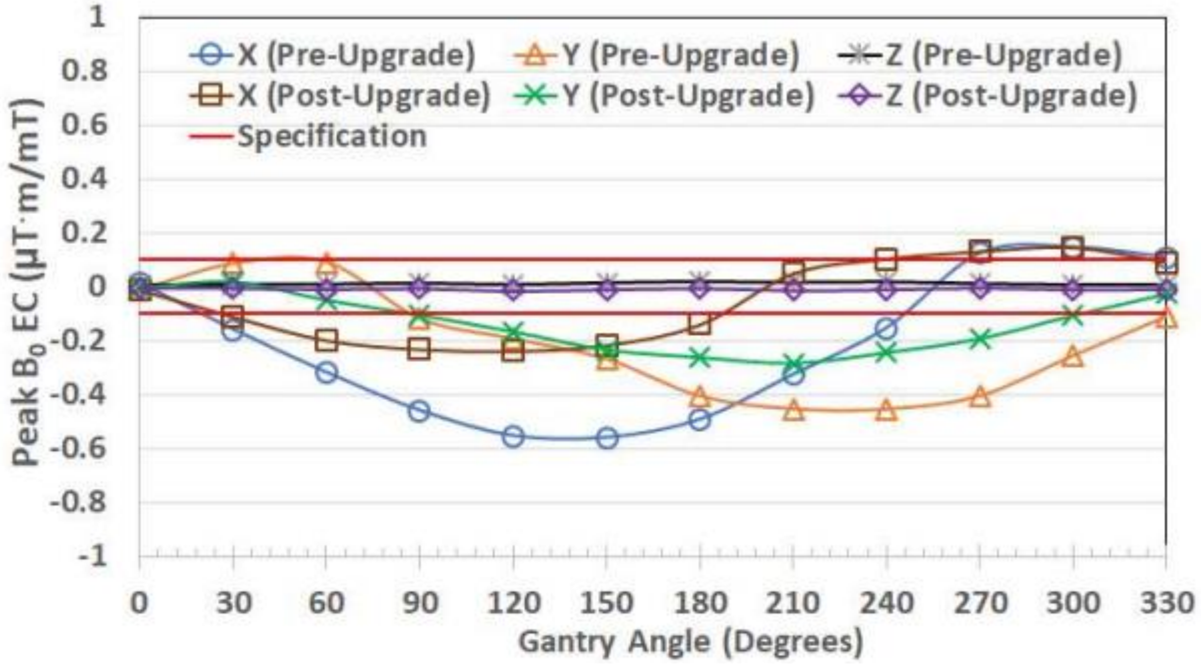

Figure 2.5: Comparison of peak B_0 eddy currents for delays < 10 ms, measured before and after the Linac RF waveguide upgrade using the slice selective excitation. Most B_0 eddy currents associated with the X and Y gradients did not meet the specification (region between red lines). The peaks are lower than the peaks in Fig. 2.4 since the nonselective excitation can sample at shorter delay times at which the B_0 eddy currents are typically larger in magnitude.

2.3.2 Gradient Eddy Currents

The peak gradient eddy currents derived from the slice-selective acquisitions are shown in Fig. 2.5. All of the gradient eddy currents were within the vendor's specification. RMS peak gradient eddy currents dropped 10.68% (P = 0.048) after the upgrade.

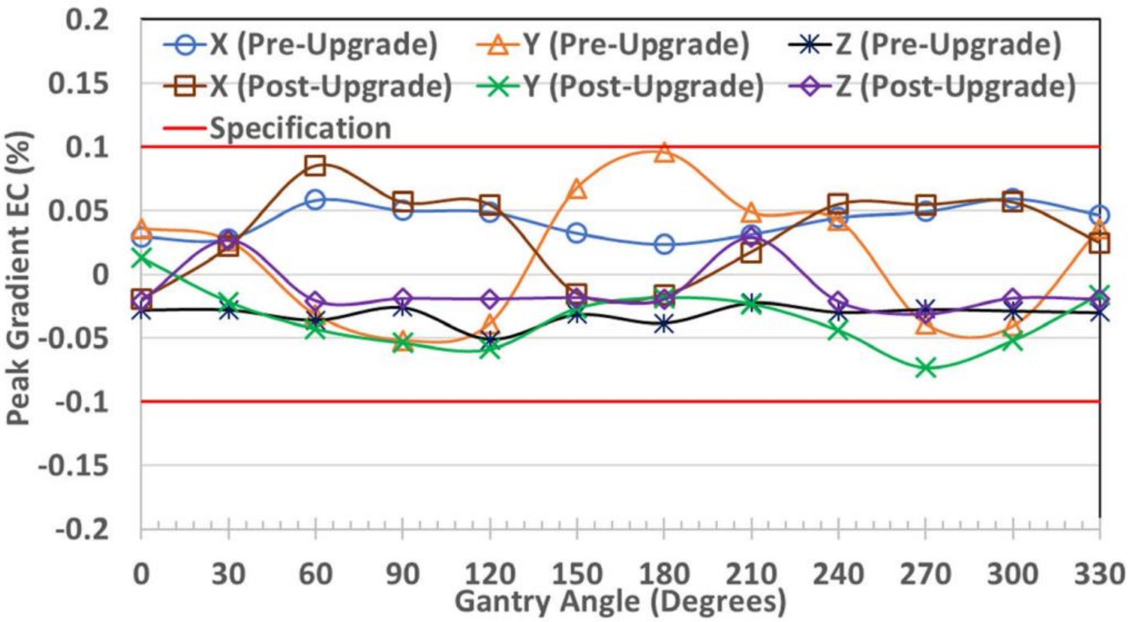

Figure 2.6: Comparison of peak amplitudes of gradient eddy currents for delays <10 ms measured before and after the Linac RF waveguide upgrade. All eddy currents were within the vendor's specification (region between red lines).

2.3.3 B_0 Inhomogeneity

The center frequency and FWHM of each spectrum and gantry angle are shown in Fig. 2.6. Center frequency offsets were < 26 Hz while B_0 inhomogeneities were < 33 Hz full width at FWHM. Both decreased after the waveguide upgrade. In principle, B_0 should be zero since the system was retuned before each acquisition. However, the tuning prescan procedure uses a stimulated-echo acquisition mode (STEAM) sequence with selective excitation while the FID sequence uses a nonselective RF pulse so the center frequency may vary between the two.

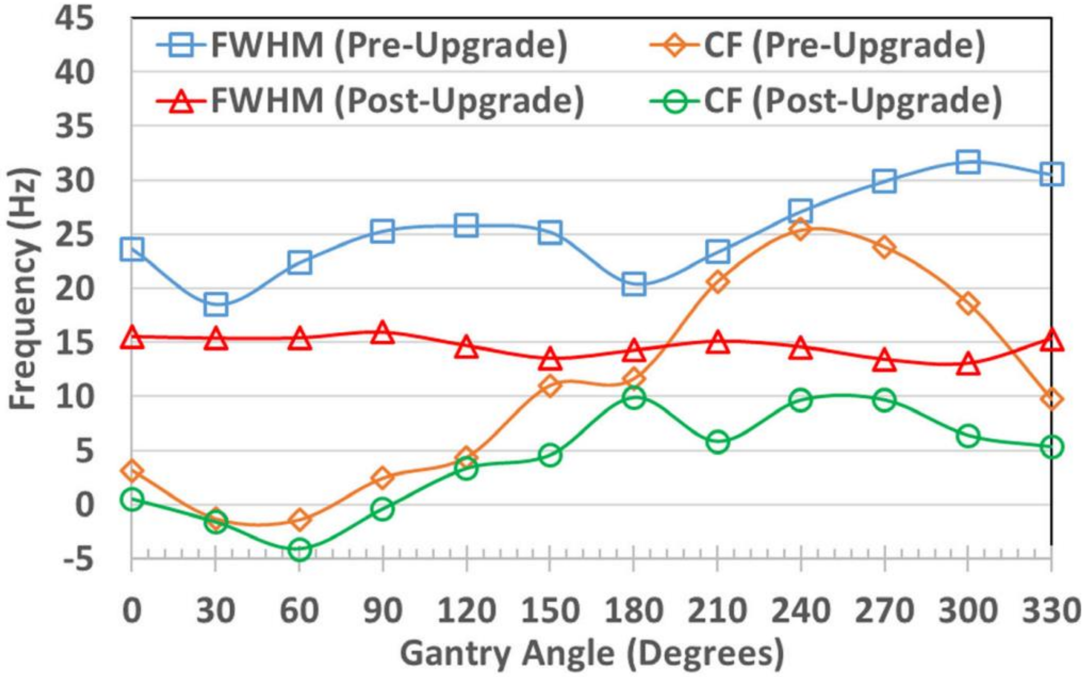

Figure 2.7: Comparison of center frequency (CF) offsets and FWHM before and after the waveguide upgrade. Data were acquired after reshimming and retuning the MRI for each gantry angle.

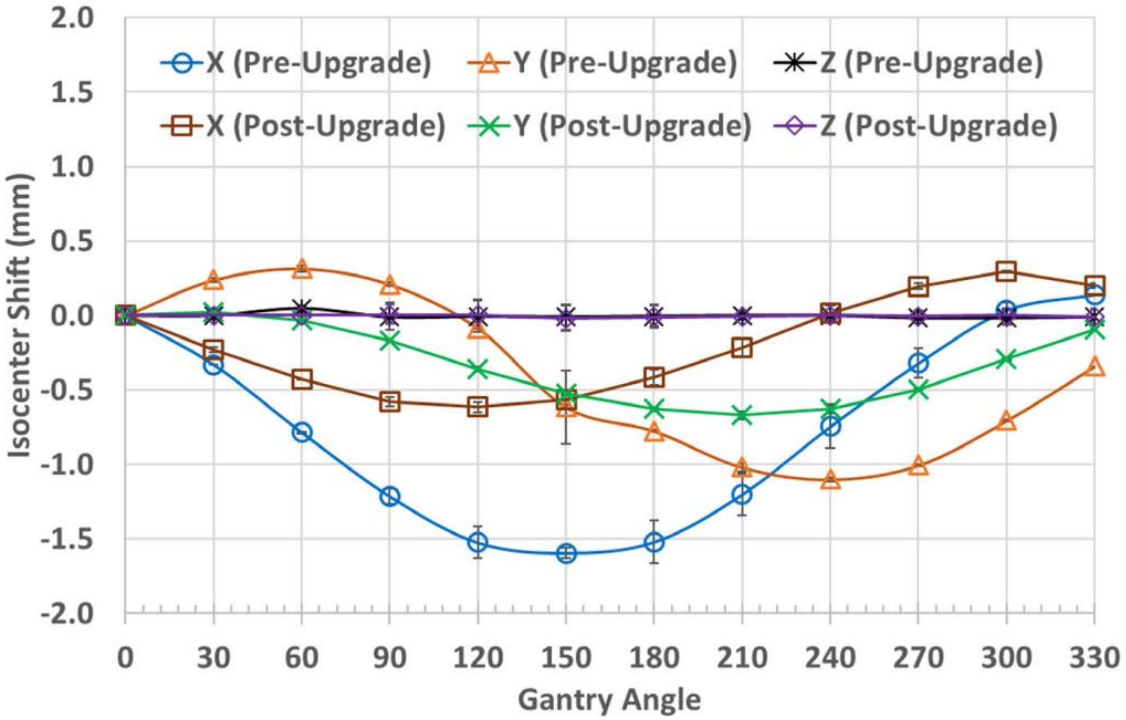

Figure 2.8: Averaged imaging isocenter shifts relative to gantry angle 0° measured from the uniformity linearity phantom. Error bars represent the standard deviation of the measurements.

2.3.4 Imaging Isocenter Shifts

Figure 2.8 shows the averaged imaging isocenter shifts derived from the uniformity linearity phantom. The shift uncertainties were generally ≤ 0.03 mm. Isocenter shifts were measured with the Y gradient as the phase encode gradient (sagittal and axial phantom orientations), the Z gradient as the readout gradient (sagittal and coronal phantom orientations), and the X gradient as phase encode (coronal phantom orientation) and readout (axial phantom orientation) gradient.

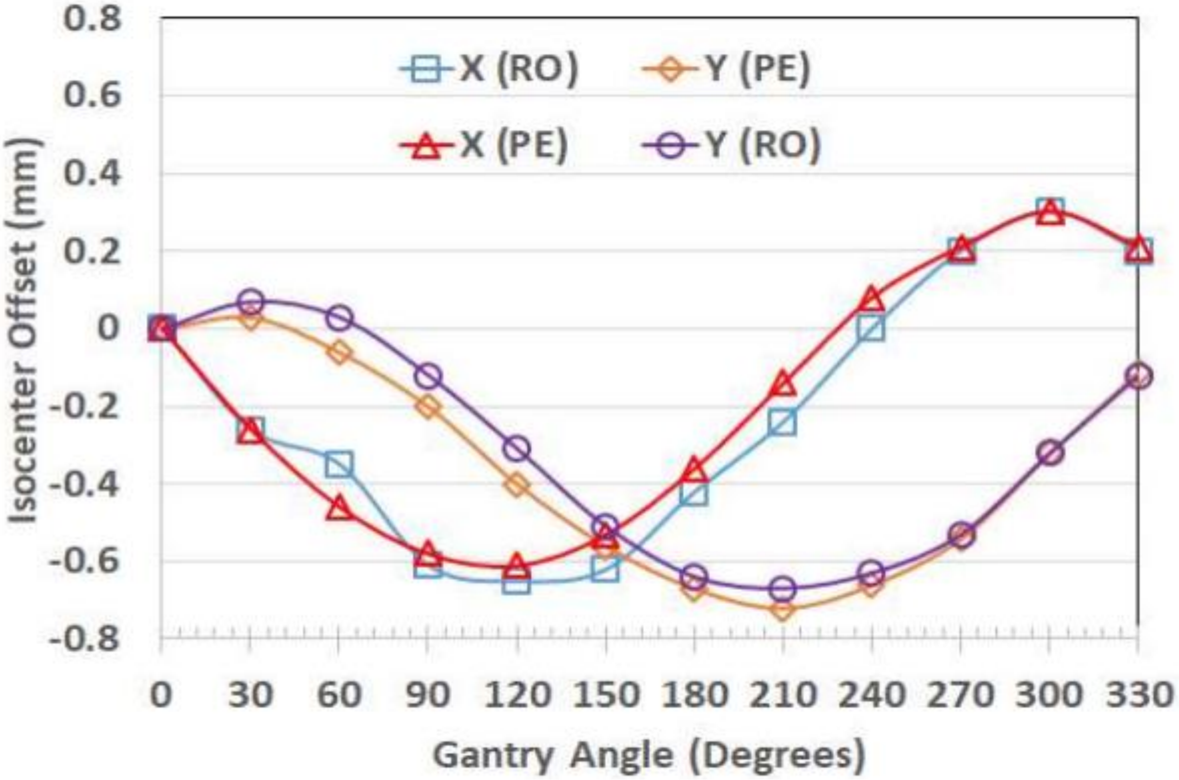

Fig. 2.9: Effects of swapping the readout (RO) and phase encode (PE) gradients (X and Y, respectively) on imaging isocenter shift for axial acquisition. The data was acquired after the waveguide upgrade using the 3D TrueFISP sequence.

Imaging isocenter shifts were measured post-upgrade to assess the effects of swapping the readout (RO) and phase encode (PE) axes (Fig. 2.9). For the axial orientation, the difference in the isocenter shift was ≤0.1 mm. It was not possible to process the sagittal and coronal data since swapping the RO and PE axes resulted in null band artifacts that prevented the analysis software from identifying the fiducial markers (Fig. 2.10).

RMS imaging isocenter shifts dropped 52.89% ($P < 0.002$) as a result of the Linac waveguide upgrade. Uncorrected mean spatial nonlinearities were 0.35 mm pre-upgrade and 0.39 mm post-upgrade for a 35-cm diameter intersecting volume. We suspect the slight rise in spatial nonlinearities was caused by the gradient recalibration during the upgrade since the gradient eddy currents decreased after the upgrade.

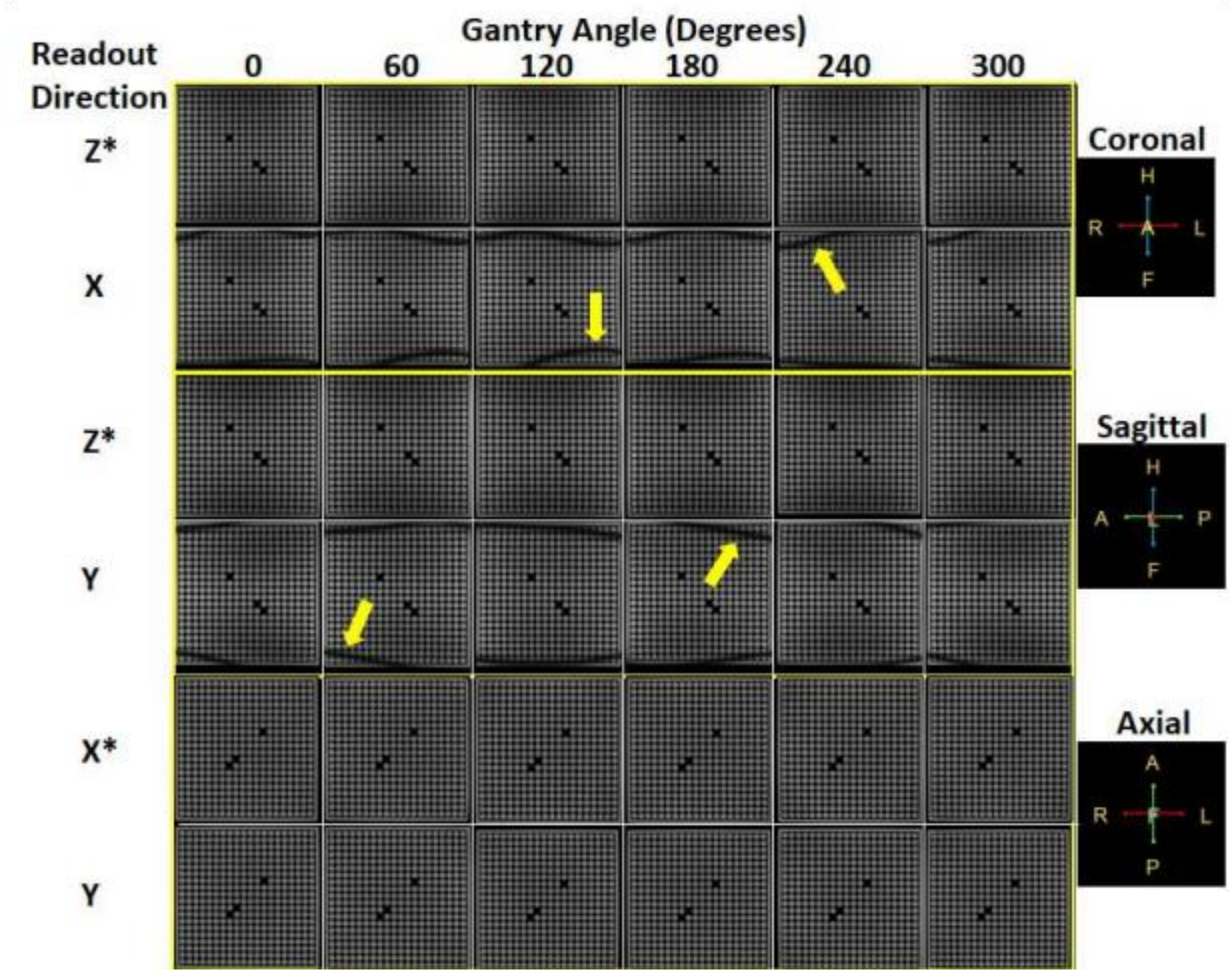

Fig. 2.10: Effects of swapping readout (RO) and phase encode (PE) direction on image artifacts for the three orthogonal uniformity linearity phantom orientations (shown at right). The nominal readout gradient axis is indicated by an asterisk for each orientation. Null band artifacts (indicated by arrows) arose when the readout direction was swapped in the coronal (RO: X) and sagittal (RO: Y) orientations. The null band artifacts caused the spatial integrity software to fail. The data was acquired after the waveguide upgrade using the 3D TrueFISP sequence.

Scatter plots showing the peak B_0 and gradient eddy currents showing the peak B_0 and gradient eddy currents (for < 10 ms, both pre- and post-upgrade) vs the measured isocenter shifts are shown in Fig. 2.11. The correlation between B_0 eddy currents and isocenter shifts was 0.965 ($P << 0.001$). If we remove the Z axis data since the isocenter shifts are minimal, the correlation was 0.961 ($P << 0.001$). The correlation between gradient eddy currents and isocenter shifts was -0.315 ($P = 0.007$) with the Z axis data and -0.360 ($P = 0.012$) without the Z axis data.

2.4 Discussion

MRgRT requires high spatial accuracy from the MRIs while minimizing image artifacts. The objective of this study was to test the hypothesis that B_0 eddy currents were the dominant cause of imaging isocenter shifts measured on the ViewRay MRI-Linac. We used the process of elimination since there were three possible contributors to isocenter shifts: (a) B_0 inhomogeneities and center frequency offsets; (b) gradient eddy currents; and (c) B_0 eddy currents.

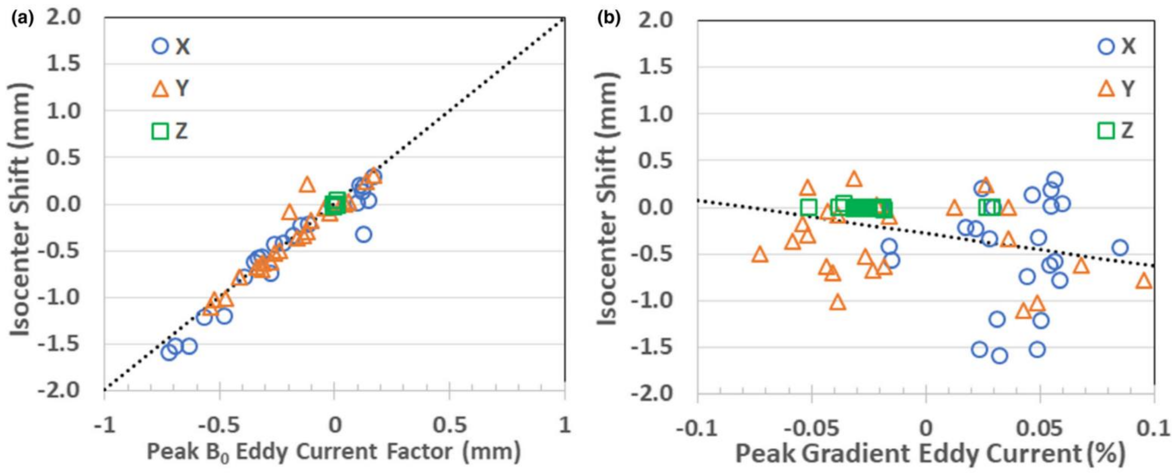

Figure 2.11: Scatter plots of isocenter shifts vs peak B_0 (a, using nonselective excitation) and gradient (b) eddy currents. A high correlation (0.965) was observed

between the isocenter shifts and the B_0 eddy currents. A low correlation (−0.315) was observed between the isocenter shifts and the gradient eddy currents.

B_0 inhomogeneities and center frequency offsets were dismissed as the main cause of the isocenter shifts due to: (a) The measured inhomogeneities were too small (Fig. 2.6); (b) The direction of the measured isocenter shifts did not reverse in our study when the readout gradient was inverted (Fig. 2.12); and (c) isocenter shifts were observed in both the readout and phase encode directions (Fig. 2.9). Based on our field homogeneity measurements, we estimate that the isocenter shifts resulting from B_0 off-resonances were < 0.1 mm for our study.

The direction of isocenter shifts from B_0 inhomogeneities changed with the polarity of the readout gradient after adjusting the center frequency of the MRI. We also verified that adjusting the center frequency did not cause shifts in the phase encode direction.

Gradient eddy currents were dismissed as the main cause of isocenter shifts based on their: (a) low magnitude and conformance with specifications; (b) low correlation with the isocenter shifts; (c) compliance of spatial integrity measurements at all tested gantry angles; and (d) localized shifts from gradient eddy currents cancel in a symmetric object that is centered at isocenter. The worst-case localized shift from gradient eddy currents during the readout would be < 0.2 mm at the lateral edge of the phantom based on our gradient eddy current measurements.

B_0 eddy currents appeared to be the primary cause of the isocenter shifts because: (a) there was high correlation between the shifts and the B_0 eddy current factors; (b) the shifts were in the order of the peak B_0 eddy current factors; (c) the shifts were consistent with the model, occurring in both the readout and phase encode directions; and (d) the shifts were not affected by inverting the gradients (Fig. 2.12).

Unfortunately, we cannot estimate readout isocenter shifts directly from the measured B_0 eddy current factors since the eddy current measurement delays (>0.7 ms) were longer than the time between the readout gradient ramp and the echo center (0.5 ms). According to Fig. 2.8, the isocenter shifts were consistently higher than our peak B_0 eddy current factors. As illustrated in Fig. 2.3, the B_0 eddy current magnitude is typically higher at shorter delay times.

The waveguide replacement reduced both the magnitude of the isocenter shifts and the B_0 eddy currents. The isocenter shifts are now less than the 1 mm. However, the B_0 eddy currents remain out of specification. B_0 eddy currents exacerbate null band artifacts in TrueFISP so further reductions in gantry-dependent B_0 eddy currents are warranted.[37,40] Enhancement of image fidelity through the reduction of eddy currents may contribute to enhanced system performance to support MRgRT and SRS.

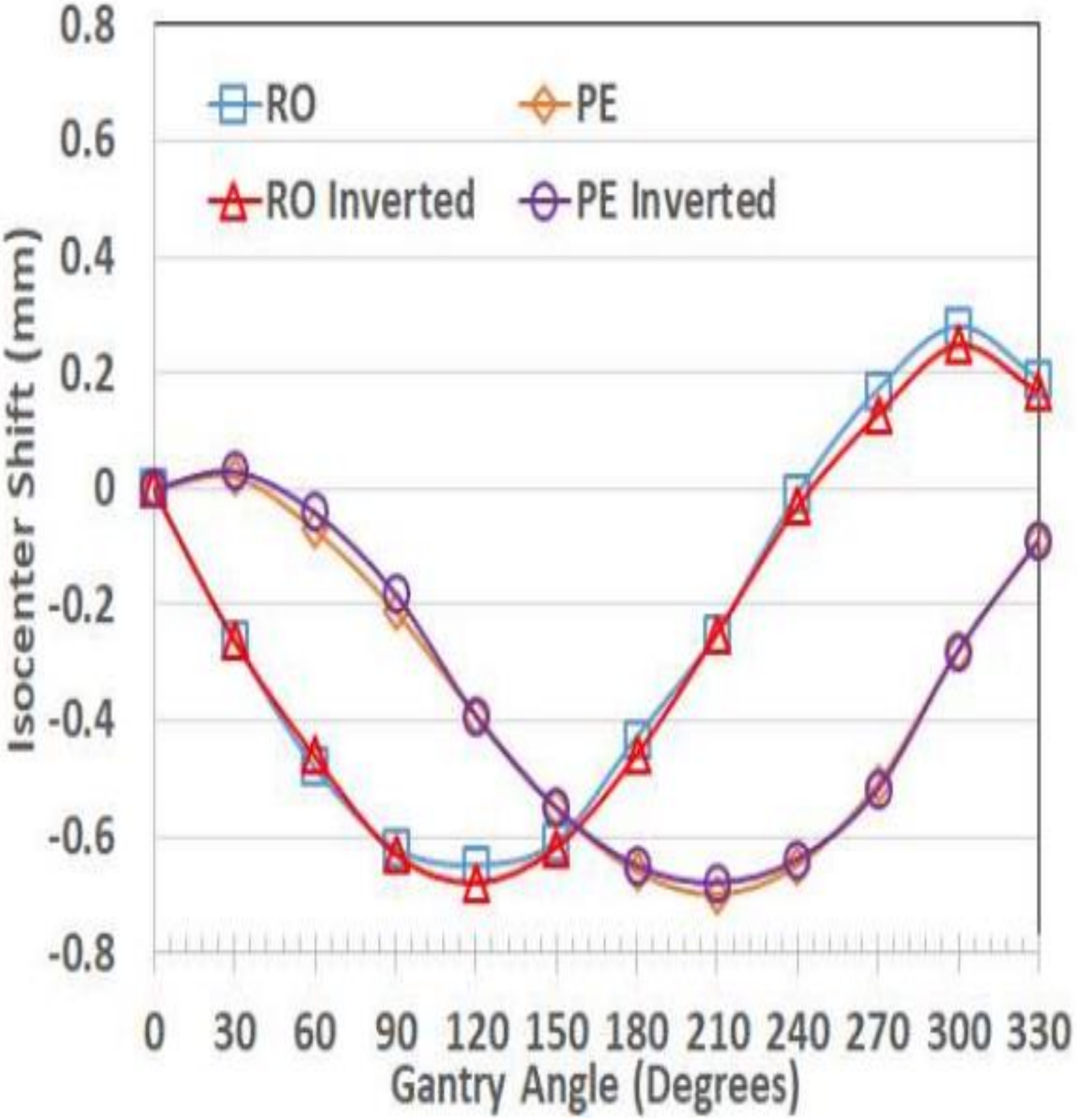

Fig. 2.12. Reversing the polarity of the readout (RO) and phase encode (PE) gradients (X and Y, respectively) had minimal effects on imaging isocenter shifts for the axial acquisition. The data was acquired after the waveguide upgrade using the 3D TrueFISP sequence.

ViewRay developed compensation for gantry angle-dependent field inhomogeneities and center frequency variations to mitigate image artifacts.[41] In principle, dynamic eddy current measurement and compensation methods developed for diagnostic MRI can be adapted for MRI-Linacs to minimize gantry angle-dependent variations in eddy currents, field inhomogeneities, and center frequency variations.[42,43]

Until gantry angle-dependent eddy current compensation is available, 3D MRIs used in treatment planning and patient setup should be acquired at the (home) gantry angle at which: (a) Eddy currents and field homogeneities are within specification (e.g., calibrated); and (b) Relative isocenter shifts over the full range of gantry angles are minimized. We are aware of significant gantry angle-dependent variations in field homogeneity and center frequency between ViewRay sites. Eddy currents and the quality of their compensation may also vary by site. Therefore, each site should know their system's gantry angle-dependent variations in field homogeneity, center frequency, eddy currents, and isocenter shifts prior to selecting their home gantry position. Studies of site-specific MRI-Linac variations would be instructive for developing solutions to imaging issues.

3D MRIs on ViewRay are typically acquired using an axial orientation. Since the Z axis was associated with small eddy currents, sagittal and coronal imaging would appear to be optimal. However, coronal 3D MRI on the ViewRay are vulnerable to parallel imaging (GRAPPA) artifacts from the low receive coil density in the anterior/posterior direction. In addition, field inhomogeneities distal to isocenter (along Z) cause image distortion on sagittal and coronal images for large fields of view. 2D cines are currently limited to the sagittal orientation for motion tracking.

The nonselective sequence provided a less noisy signal when measuring B_0 eddy currents compared with the slices-selective sequence. Additionally, the shorter delays in the nonselective sequence made it preferable for measuring B_0 eddy currents with shorter time constants. Both sequences have the advantage that they do not require specialized hardware or phantoms to run.

There are a couple of limitations with this study. First, we limited the eddy current characterization to short time constant eddy currents. The 2D and 3D TrueFISP sequences used in treatment planning and real-time treatment have gradient pulse durations of 0.3-2 ms which is significantly shorter than the 10-ms gradient pulse used to stimulate eddy currents in this study. Therefore, these sequences should not stimulate eddy currents beyond those studied herein. Second, we did not measure cross-term eddy currents in this study since we expect them to be significantly smaller than the gradient eddy currents. Thus, cross-term eddy currents were not a concern given that gradient eddy currents were within specification and not a primary cause of isocenter shifts. Nevertheless, this is the first study to quantify eddy currents in an MRI-Linac.

2.5 Conclusions

Imaging isocenter shifts measured in a commercial 0.35 T MRI-Linac were highly correlated and consistent with B_0 eddy currents, particularly for gradient waveforms played out along the X and Y axes. The redesign of the RF waveguide to increase its distance from the magnetic field resulted in a significant drop in B_0 eddy currents and imaging isocenter shifts. However, B_0 eddy currents remain outside of the Siemens specification along the X and Y axes.

Chapter 3: Real-time B_0 compensation during gantry rotation in a 0.35 T MRI-Linac

This chapter has been published Medical Physics. 2022 Oct;49(10):6451-6460. doi: 10.1002/mp.15892.. Text, figures, equations, and references have been modified from the published work for consistency.

3.1 Introduction

Commercial MRI–Linacs are currently restricted to step-and-shoot IMRT meaning that both the gantry and MLCs are stationary while the beam is turned on.[9–12] This delivery method avoids image artifact and tracking issues associated with electromagnetic interference (EMI) created during MLC motion or gantry rotation in MRgRT systems. However, restricting treatment to step-and-shoot IMRT may result in longer treatment times or reduced target conformality compared to VMAT.[44,45] VMAT enables dose delivery while the gantry is rotating and the MLCs are moving.[19,20] Additionally, VMAT can improve dose conformality.[21]

Artifact-free imaging during radiation therapy is an important step toward implementing MRI-guided arc therapy on MR-IGRT systems. Previous studies showed that MLC motion did not produce significant EMI that impacted MRI quality on the two FDA-approved commercial MRI–Linac models.[41,46] However, large B_0 fluctuations that can produce image artifacts and imaging isocenter shifts were reported for a commercial 0.35 T MRI–Linac during gantry rotation.[18,47] These B_0 fluctuations potentially constitute a key obstacle to performing MRI-guided VMAT.

Balanced steady-state free precession (bSSFP) sequences are typically used for real-time imaging during MR-IGRT treatment due to their high signal-to-noise ratio (SNR) and high temporal resolution. However, bSSFP sequences are sensitive to B_0 fluctuations. Off-resonances of ±1/(2*TR), where TR is the repetition time, result in bands of signal loss (dephasing) known as null bands.[48] Significant null band artifacts have been previously reported during gantry rotation on a 0.35 T MR-IGRT system.[22] Null band artifacts were primarily attributed to sinusoidal B_0 fluctuations during gantry rotation resulting from interaction between the main magnetic field and the six gantry-mounted ferromagnetic MuMetal shield buckets spaced every 60°. Additionally, center frequency offsets can result in image isocenter shifts, potentially leading to misalignment between the imaging and radiotherapy isocenters and dosimetric errors.[18]

Real-time prospective B_0 corrections were previously demonstrated for diagnostic MRI systems.[49] Free induction decay (FID) navigators were used prospectively to correct B_0 fluctuations.[50] Small frequency shifts associated with diffusion-weighted MRI were resolved by adjusting the RF pulse and receiver frequencies in real time after the center frequency shift was calculated from the phase correction lines acquired during the echo planar imaging readout.[51] External and internal field probes were also used to measure B_0 fluctuations with the results fed back into a B_0 correction coil or the pulse sequence.[42,52] Typically, the previous methods were designed for B_0 fluctuations of <50 Hz.[53] By contrast, gantry rotation B_0 variations spanned a range of ±400 Hz.[22]

The objective of this study was to demonstrate the feasibility of using FID navigators to prospectively (in real time) correct center frequency offsets of ±400 Hz and minimize image variations and artifacts due to gantry rotation on a low magnetic field MRI–Linac.

3.2 Material and Methods

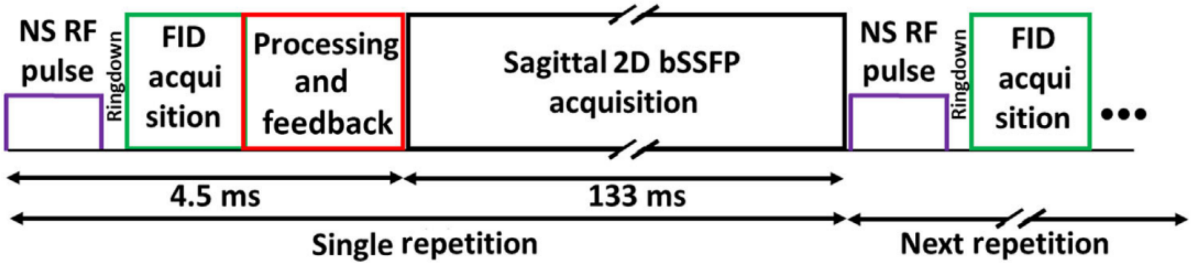

Figure 3.1: The modified balanced steady-state free precession (bSSFP) sequence with an added nonselective (NS) free induction decay (FID) navigator. The FID navigator runs immediately before the corrected image acquisition. A nonselective (rectangular) pulse generates an FID from which the center frequency offset is measured and fed back to the pulse sequence for correction of the selective excitations and receiver frequencies in the adjacent image acquisition. Each bSSFP acquisition includes a steady-state preparation consisting of variable flip angle excitations. The gradients in the steady-state preparation dephase the FID to avoid interference with the image acquisition. Note the timing is not drawn to scale.

Experiments were performed on a 0.35 T MRI–Linac (ViewRay MRIdian, Oakwood Village, OH) running software version 2.0.2. The MRI subsystem ran Siemens IDEA/ICE version VB19 software for pulse sequence execution and image reconstruction. All scans were performed using the “MRI QA” mode of the MRI–Linac to allow for the use of modified pulse sequences and ICE using two (posterior and anterior) six-channel flexible torso coils. Each torso coil has three coil elements in the lateral direction by two coil elements in the cranial–caudal direction. Shimming was performed for all scans at the initial gantry position prior to each gantry rotation.

To measure center frequency fluctuations, an FID navigator employing a nonselective (rectangular) RF excitation pulse (flip angle: 35°, RF duration: 500 μs, acquisition dwell time:8 μs,64 complex data points) was integrated into a 2D Cartesian bSSFP cine sequence (Figure 3.1). A delay of 100 μs was added after each navigator RF pulse and prior to the FID acquisition to protect the receiver from RF coil ring-down. The first FID navigator served as the center frequency reference. Each subsequent FID navigator was used to estimate the center frequency offset (Δf) according to the following equation:

$$\Delta f = \frac{1}{2\pi}\left(\frac{\mathrm{d}\phi_{new}}{\mathrm{d}t} - \frac{\mathrm{d}\phi_{ref}}{\mathrm{d}t}\right) \quad (3.1)$$

where ϕ_{new} and ϕ_{ref} are, respectively, the current and reference phase unwrapped (unaliased) FID navigator phases. We only used the FID signal from the superior–anterior center RF coil element for the Δf calculations. The first 9 and last 10 data points from each FID were discarded to reduce variance. The measured center frequency offset was then sent from the ICE computer back to the pulse sequence as a real-time feedback object. The navigator processing required a 3 ms pause in the sequence execution for the real-time feedback.

Once the center frequency offset was received by the pulse sequence, the transmit/receive frequency for the sagittal 2D bSSFP acquisition (echo/repetition times: 1.09/2.18 ms, flip angle: 70◦, field of view: 350 × 350 mm^2, Matrix: 100 × 100, slice thickness: 7 mm, bandwidth: 1515 Hz/pixel, partial k-space: 75%, slices: 1, averages: 1, generalized autocalibrating partially parallel acquisitions (GRAPPA) factor: 2, frame rate: 7.3 frames/s) was adjusted to account for the change in the center frequency associated with gantry rotation if B_0 compensation was enabled. The transmitter/receiver phase was adjusted for each excitation using the following equation:[54]

$$\phi_n = (n-1) \cdot \Delta f \cdot TR \cdot 360^\circ + \phi_{cycle} \quad (3.2)$$

where ϕ_n gives the phase increment in degrees for the nth excitation. TR is the repetition time, Δf is the central frequency offset obtained from the previous navigator measurement, and ϕ_{cycle} represents the alternating phase (0° and 180°) for maintaining the balanced steady state.

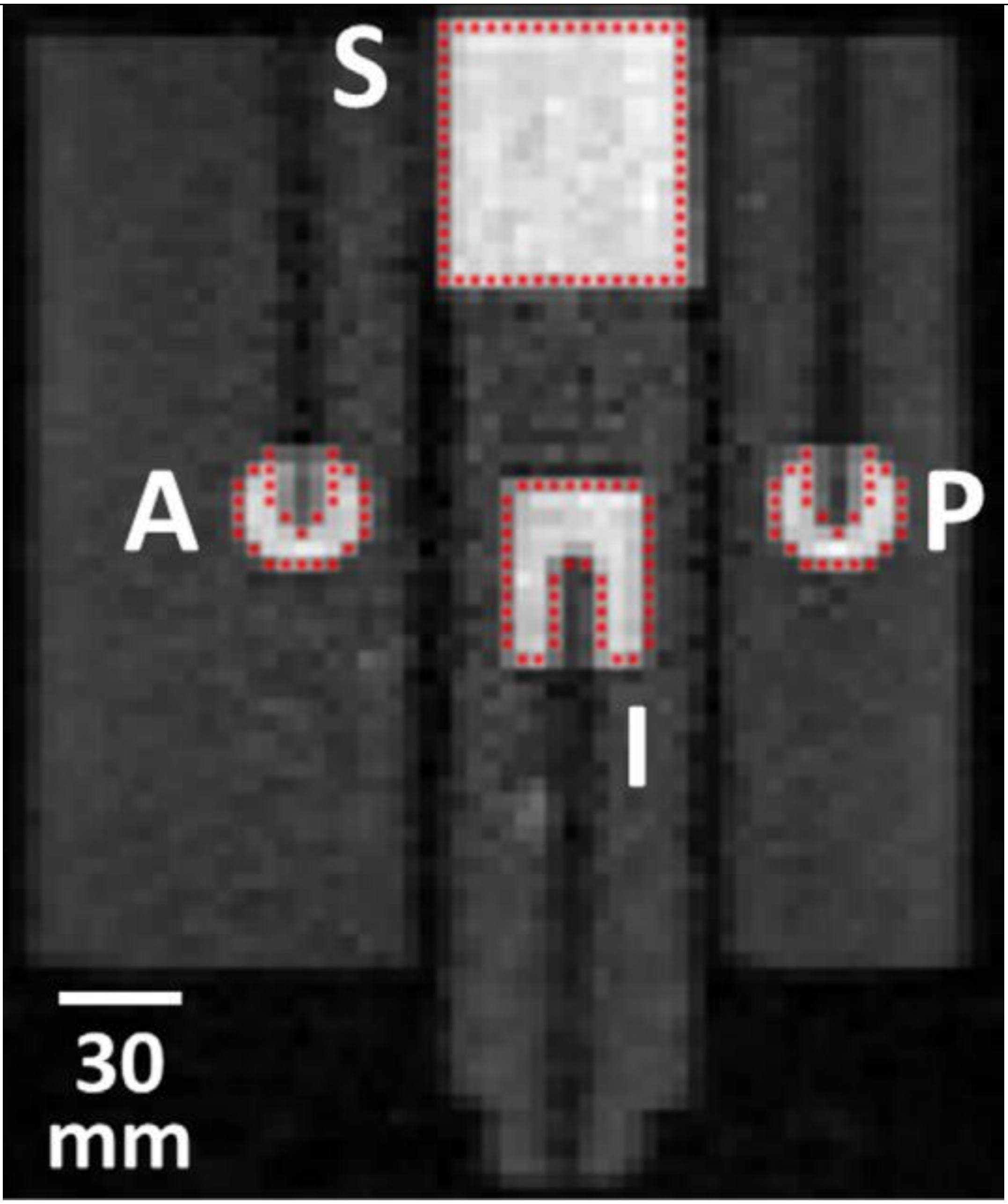

Figure 3.2: Sagittal FID navigator bSSFP MRI of stationary CIRS phantom with manually drawn reference contours shown in red on each of the anterior (A), superior (S), inferior (I), and posterior (P) targets.

3.2.1 Phantom Measurements

An MRI–Linac dynamic phantom (CIRS, Norfolk, Virginia) was imaged using the 2D FID navigator bSSFP cine sequence with and without B_0 compensation. Images were acquired with the phantom remaining stationary while the gantry rotated fully clockwise (CW) starting at 33° (33°→90°→180°→270°→0°→30°), and with the gantry rotated fully counterclockwise (CCW) starting at 30° (30°→0°→270°→180°→90°→33°). The gantry cannot travel to 31° or 32° due to the Linac gantry mechanical design, so these rotations represent the entire range of allowable gantry angles. The gantry rotation speed was previously measured at 3.42°/s (0.060 rad/s) when not accelerating or decelerating.[22] FID navigators were acquired for images with and without B_0 compensation, and the center frequency offsets were calculated. The offsets allowed the cine frames without B_0 compensation to be properly aligned retrospectively for comparison with the cine frames using real-time B_0 compensation.

The target tracking feature on the MRI–Linac was only available in RT mode using unmodified pulse sequences and reconstructions. Therefore, to simulate tracking, the four MRI targets in the CIRS phantom were manually contoured on the first cine image of each acquisition retrospectively in MATLAB version R2019a (Figure 3.2), and an active contouring algorithm was applied to each subsequent frame using the manually drawn contour as the initial template.[55] Dice coefficients between each active contour and the corresponding initial manual contour were calculated for the B_0 corrected and uncorrected images acquired during gantry rotation. Because the phantom did not move, the ideal Dice coefficient is 1, which suggests perfect overlapping between the active contour and the initial manual contour. For each frame, the normalized root mean square error (nRMSE) was calculated for a region of interest (ROI) encompassing the phantom using the mean from a reference image that was acquired before gantry rotation. Paired t-tests between measurements with and without B_0 compensation were conducted for the Dice coefficients and nRMSEs. The SNR was calculated over the phantom using the two-image difference method.[56]

Based on Faraday's law, the center frequency offset should be directly proportional to the velocity of the gantry with a caveat: long time constant eddy currents produced center frequency offsets after the gantry came to rest.[18] Therefore, the gantry rotation–related center frequency offsets measured in the CIRS phantom were modeled based on the convolution of a sinusoid input function (s) and a long time constant eddy current (τ) transfer function (m) using:

$$s(t) = \left(A \cdot \left(\frac{\omega}{|\omega_{max}|}\right) \cdot \sin[6(\omega t + B + \theta_0)]\right)(u[t_{start}] - u[t_{start} - t_{end}]) + C \quad (3.3)$$

$$m(t) = \exp\left[\frac{-t}{\tau}\right] \cdot u[t] \quad (3.4)$$

$$\Delta f(t) = s(t) \otimes m(t) \quad (3.5)$$

where A–C are fitting coefficients, ω is the gantry angular velocity with the maximum ω_{max} (currently 0.060 rad/s for the MRIdian). θ_0 is the starting angle for the gantry rotation. *u* represents the unit step function with gantry rotation start and end times t_{start} and t_{end}. The factor 6 in Equation 3.3 is related to the presence of the six shield buckets in the gantry.

3.2.2 In Vivo Measurements

MRIs were performed on three healthy adult volunteers (one female and two males, ages 37–58, weights 66–75 kg) in accordance with an Institutional Review Board approved protocol using the 2D bSSFP sequence protocol both with and without B_0 compensation. The volunteers were imaged head first supine with the anterior and posterior receiver coils positioned for imaging the thorax and upper abdomen. Scans were performed with the volunteers' arms at their sides to increase volunteer comfort. Acquisitions were acquired with the gantry rotating fully CW and CCW. nRMSEs were calculated for an ROI encompassing the body with and without B_0 compensation. Paired t-tests were performed between nRMSE measurements acquired with and without B_0 compensation.

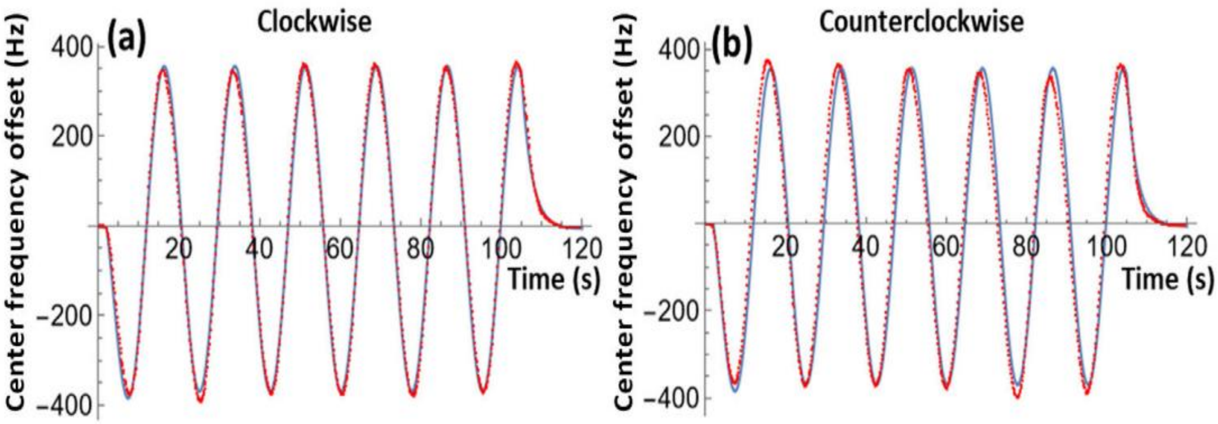

Figure 3.3: Center frequency offsets (red points) versus time measured in the CIRS phantom during clockwise (CW) gantry rotation starting at gantry angle 33° (a) and counterclockwise gantry rotation starting at gantry angle 30° (b). The blue lines represent the convolution model in Equations (3.3)–(3.5). Note that the alignment of the model and data is imperfect because we assumed a constant gantry velocity ($v = v_{max}$), thus ignoring the gantry acceleration and deceleration at the initial and final gantry angles. The sinusoidal behavior is related to the six ferrous shield buckets mounted at 60° increments around the gantry.

3.3 Results

Figure 3.3 shows the center frequency offsets measured as a function of time during CW and CCW gantry rotation in the CIRS phantom and compares the data to the convolution model. The offsets look similar as a function of time but are distinctly different when plotted versus gantry angle (Figure 3.4). For CW rotation starting at 33°, the fit values were $A = -197.530$ Hz, $B = -0.162$ rad, $C = -2.840$ Hz, $\tau = 2.438$ s, $\omega = 0.060$ rad/s with goodness of fit $R^2 = 0.995$ and root mean square error (RMSE) = 16.96 Hz. For CCW starting at 30°, the fit values were $A = 213.964$ Hz, $B = -0.037$ rad, $C = -2.718$ Hz, $\tau = 2.146$, $\omega = -0.060$ rad/s with $R^2 = 0.994$ and RMSE = 18.54 Hz.

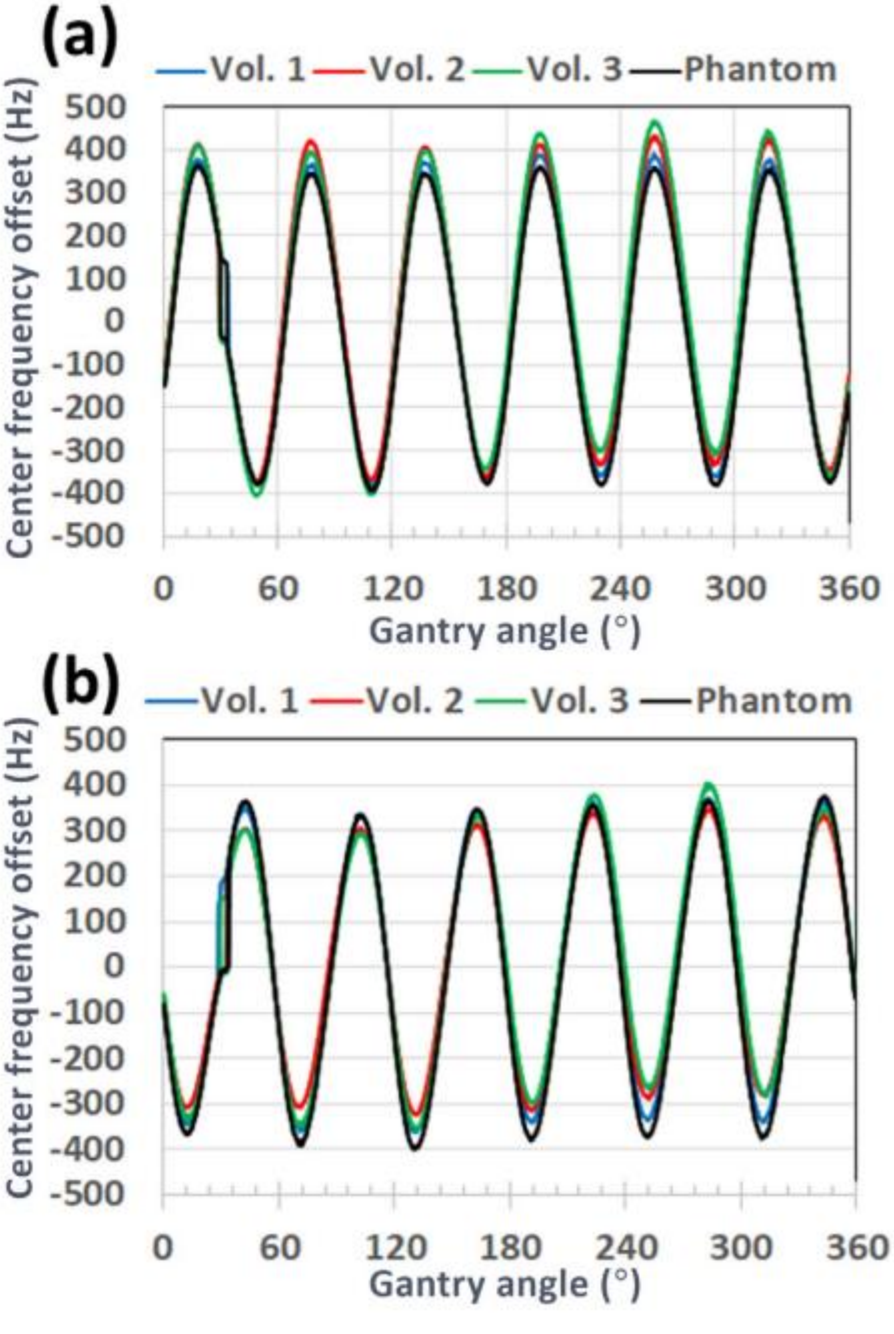

Figure 3.4: Comparison of center frequency offsets measured using free induction decay (FID) navigators in three volunteers and the CIRS phantom during clockwise (CW) (a) and counterclockwise (CCW) (b) gantry rotation and plotted by gantry angle. The discontinuities at gantry angles 30° and 33° gantry rotations are caused by acceleration/deceleration of the gantry and long-time constant B_0 eddy currents. The gantry does not travel to angles 31° and 32° by design.

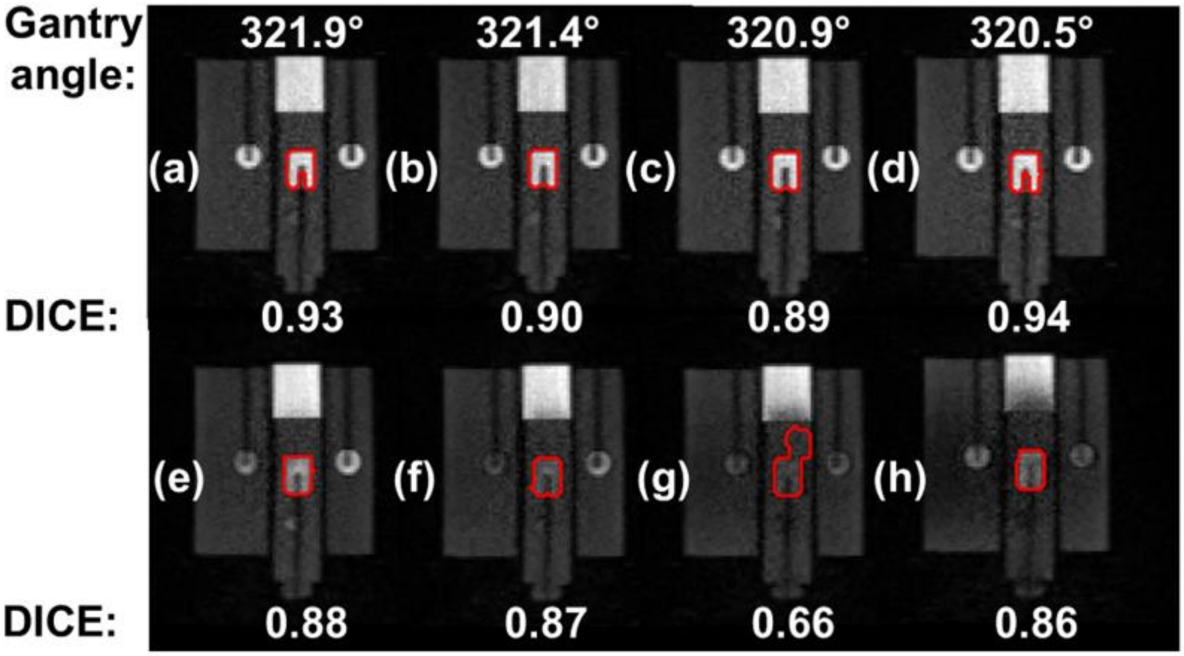

Figure 3.5: Dice coefficients calculated for the inferior contour (red boundary). Four successive frames (from left to right) of a 2D balanced steady-state free precession (bSSFP) sequence (7.3 frames per second) with real-time B_0 compensation during counterclockwise gantry rotation (a–d) in the CIRS phantom for gantry angles 320°–322°. The scan repeated without B_0 compensation suffers from artifacts and signal losses during gantry rotation (e–h).

The central frequency offsets measured during the volunteer scans were generally consistent with the phantom measurements (Figure 3.4). However, the maximum peak-to-peak (pk–pk) amplitudes of the center frequency offsets were 757 Hz (CW) and 773 Hz (CCW) in the CIRS phantom and 871 Hz (CW) and 760 Hz (CCW) in vivo. The repeatability of the FID navigator center frequency measured in the CIRS phantom was <2 Hz based on the root mean square error (RMSE) of repeated measurements. The repeatability of the center frequency offset measurements in vivo was <3 Hz (RMSE) and included variations associated with physiological motion.

Figure 3.5 shows an example of the benefits of B_0 compensation in image quality, Dice coefficient, and contour reproducibility for the CIRS phantom during gantry rotation. Due to the small sizes of the objects and the limited image resolution (Figure 3.2), a Dice coefficient ≥ 0.8 was empirically determined to be sufficient to ensure satisfactory similarity and, thus, was used as a surrogate for tracking performance.

In Figure 3.6, the Dice coefficients with versus without B_0 compensation are plotted based on gantry angle and gantry rotation direction for the four contours in the CIRS phantom (defined in Figure 3.2). All of the contours imaged with B_0 compensation had Dice coefficients >0.8. Without B_0 compensation, Dice coefficients were <0.8 from 0% to 21% of the time, depending on the contour.

Mean Dice coefficients, averaged over the entire gantry rotation, are presented in Table 3.1 based on the contour, gantry rotation direction, and the use of B_0 compensation. All paired t-tests (with vs. without B_0 compensation) had $p \ll 0.001$, thus demonstrating a significant benefit from the B_0 compensation in the phantom. However, the addition of the FID navigator resulted in a 11% drop in image SNR (from 13.00 without the navigator to 11.59 with the navigator).

Figure 3.7 illustrates the reduction in nRMSE with real-time B_0 compensation in vivo. nRMSE for the three volunteers and the CIRS phantom during gantry rotation with versus without B_0 compensation are plotted in Figure 3.8 based on gantry angle and gantry rotation direction.

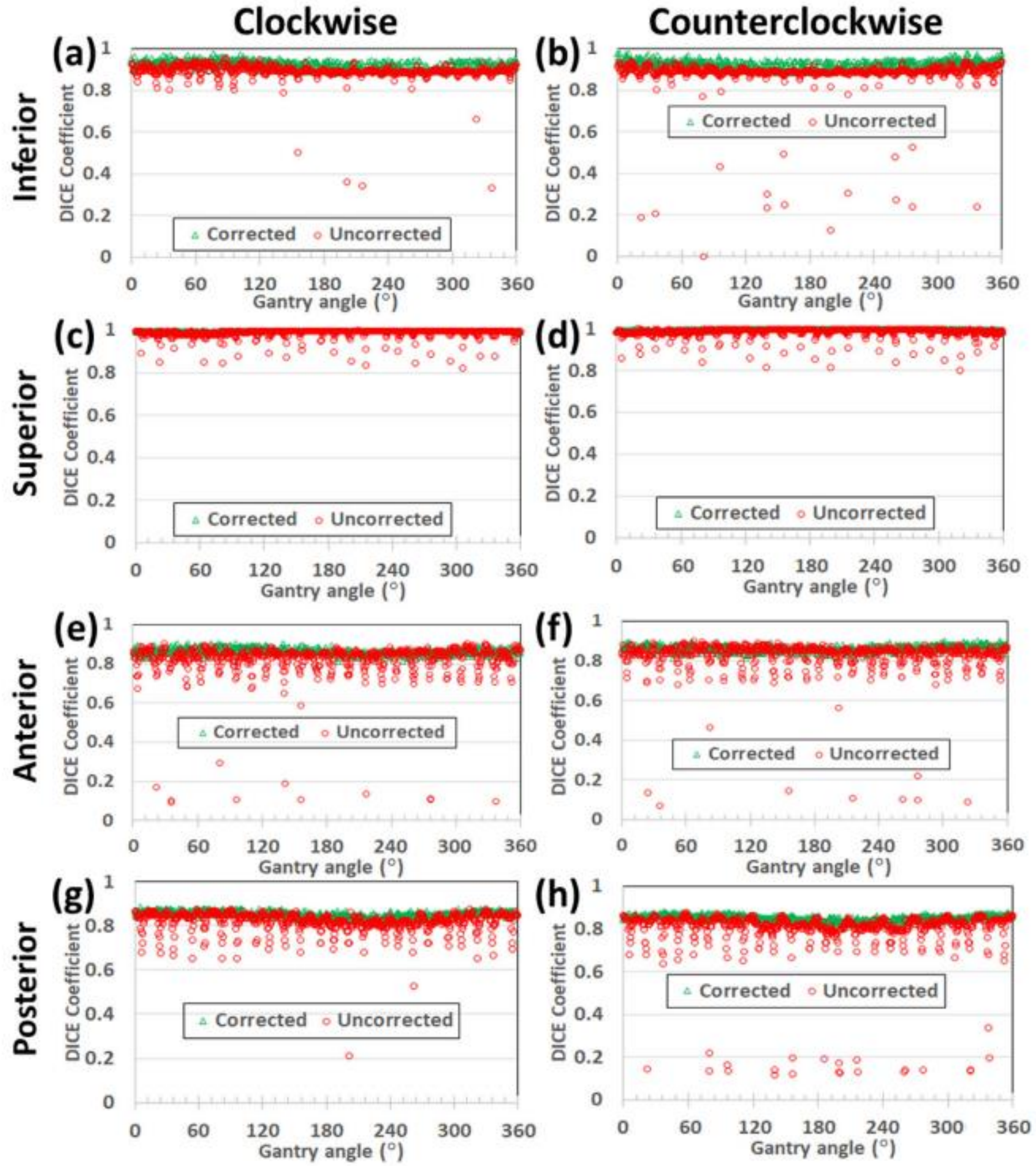

Figure 3.6: CIRS phantom results for the four contours. Dice coefficients for the inferior (a and b), superior (c and d), anterior (e and f), and posterior (g and h) contours during clockwise (CW) (a, c, e, and g) and counterclockwise (b, d, f, and h) gantry rotation while acquiring 2D balanced steady-state free precession (bSSFP) MRIs at 7.3 frames per second. The B_0 correction (Δ) resulted in consistent Dice coefficients compared to images acquired without real-time B_0 correction (O). The zero value at gantry angle 80° in (b) resulted from the tracking algorithm selecting the wrong target.

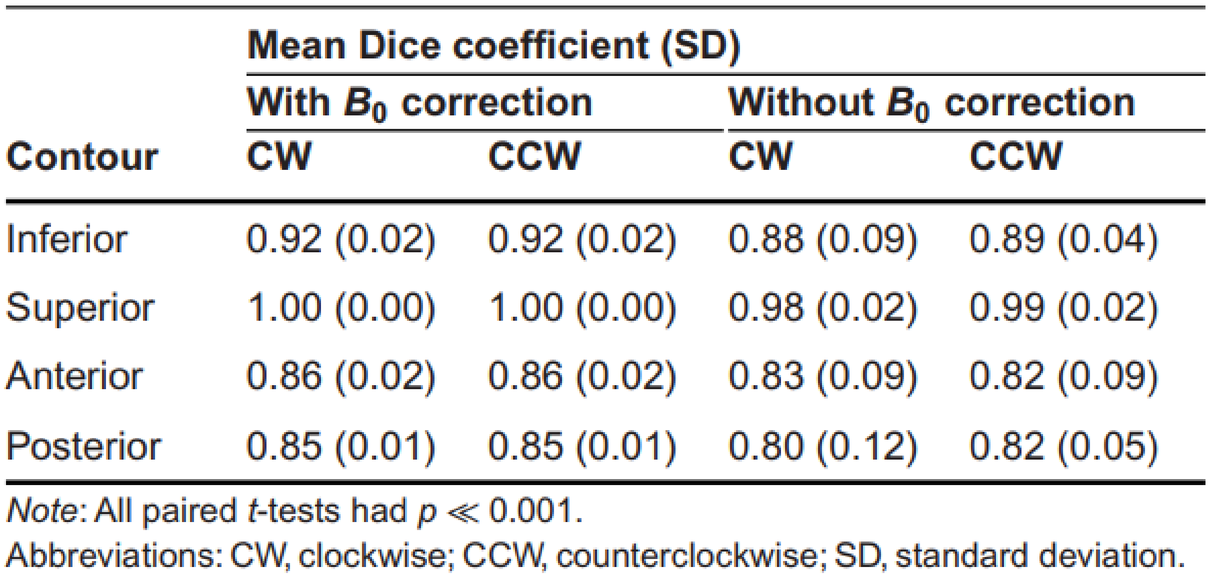

Contour	Mean Dice coefficient (SD)			
	With B_0 correction		Without B_0 correction	
	CW	CCW	CW	CCW
Inferior	0.92 (0.02)	0.92 (0.02)	0.88 (0.09)	0.89 (0.04)
Superior	1.00 (0.00)	1.00 (0.00)	0.98 (0.02)	0.99 (0.02)
Anterior	0.86 (0.02)	0.86 (0.02)	0.83 (0.09)	0.82 (0.09)
Posterior	0.85 (0.01)	0.85 (0.01)	0.80 (0.12)	0.82 (0.05)

Note: All paired *t*-tests had $p \ll 0.001$.
Abbreviations: CW, clockwise; CCW, counterclockwise; SD, standard deviation.

Table 3.1: Effects of B_0 compensation on mean Dice coefficient for each phantom contour region versus gantry rotation direction.

The changes in mean nRMSEs (i.e., averaged over the entire gantry rotation) resulting from B_0 compensation are stated for the CIRS phantom and the three volunteers in Table 3.2. Real-time B_0 compensation resulted in reductions in mean nRMSEs of 51% and 16% for the CIRS phantom and in vivo, respectively. The lower reductions in mean nRMSEs in vivo were associated with physiological motion. All paired t-tests had $p \ll 0.001$ except for Volunteer 1′s CCW gantry rotation measurements ($p = 0.51$).

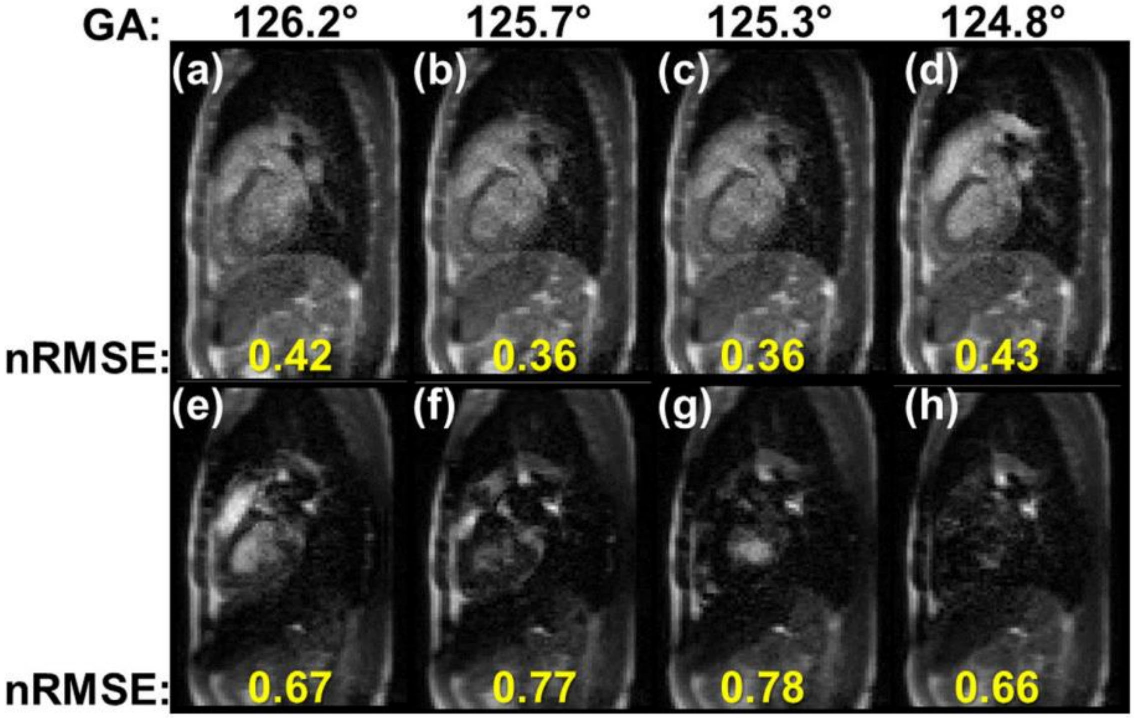

Figure 3.7: Normalized root mean square error (nRMSE) values for four successive frames from Volunteer 1 (37-year old male) using the 2D Cartesian balanced steady-state free precession (bSSFP) sequence with (a–d) and without (e–h) real-time B_0 compensation, as the radiation therapy gantry rotated counterclockwise from 126° to 125°. Significant signal dephasing and null bands are present when B_0 compensation was not used. GA, gantry angle; nRMSE, normalized root mean square error.

3.4 Discussion

The objective of this study was to demonstrate the feasibility of using FID navigators to correct center frequency offsets and minimize the effects of gantry rotation on image quality in a phantom and in vivo. The B_0 compensation generally resulted in improved image quality as indicated by a reduction in nRMSE in the phantom and human volunteers, and an increase in the Dice coefficient for the contours in the phantom.

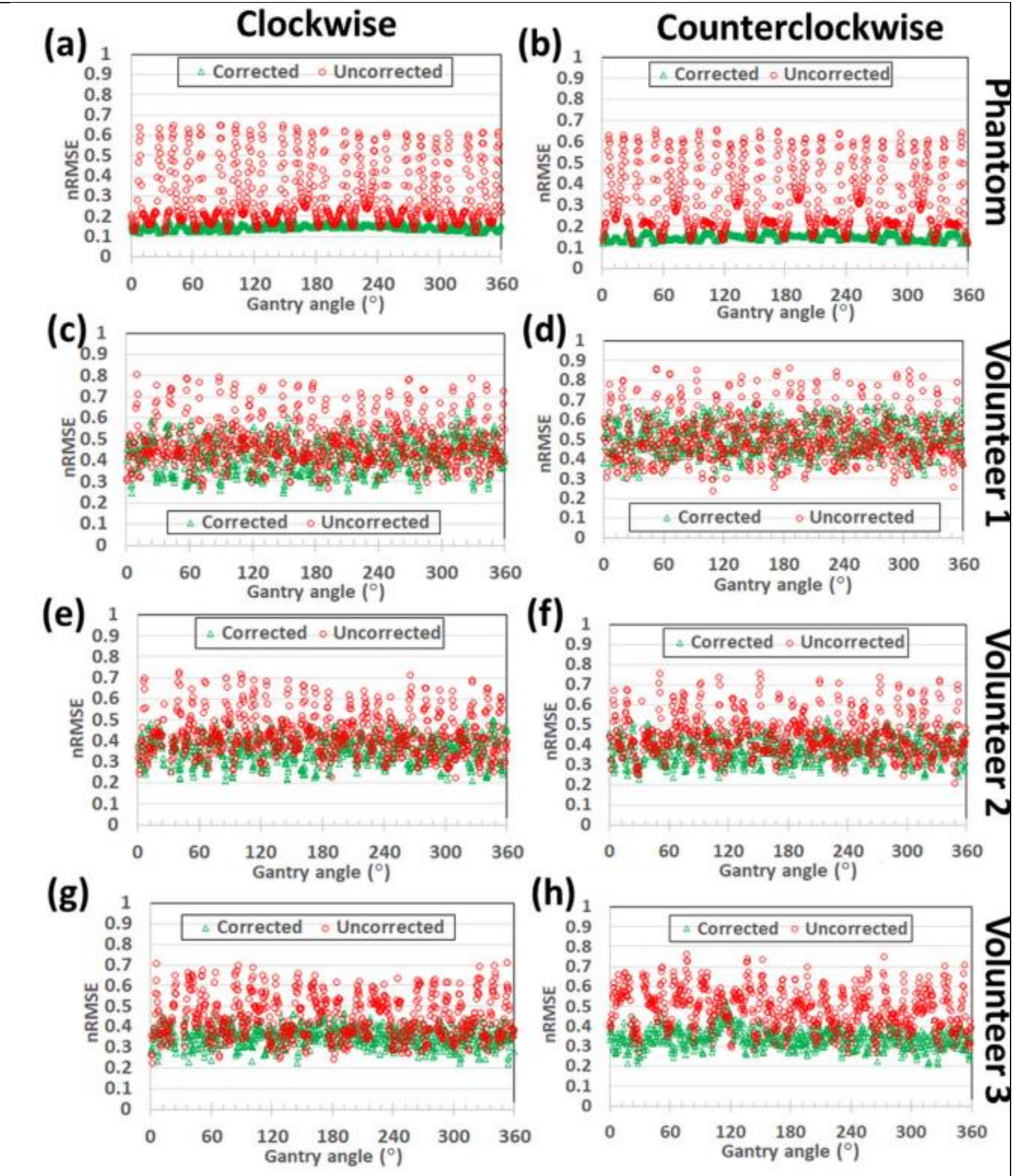

Figure 3.8: Comparison of normalized root mean square errors (nRMSEs) measured with (Δ) and without (O) B_0 compensation for clockwise (CW) (a, c, e, and g) and counterclockwise (b, d, f, and h) gantry rotation using the CIRS phantom (a and b) and in vivo for Volunteer 1 (c and d), Volunteer 2 (e and f), and Volunteer 3 (g and h).

Physiological motion causes the variance of the B_0-compensated MRIs to be higher in vivo compared to the stationary phantom

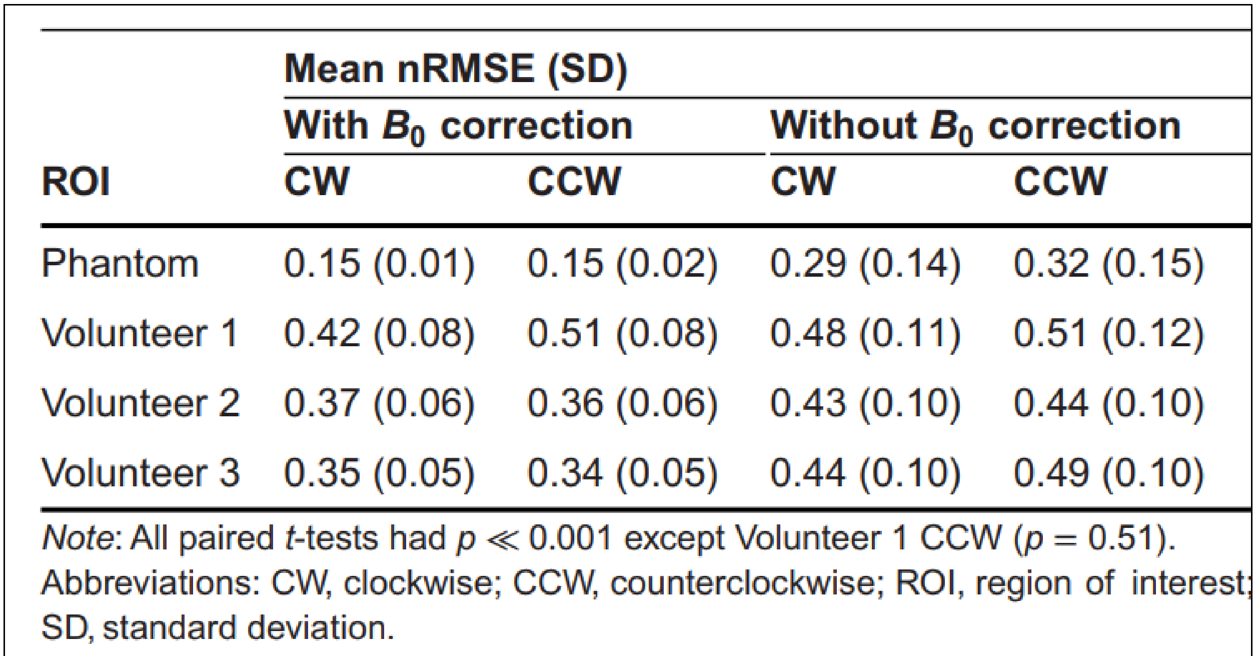

	Mean nRMSE (SD)			
	With B_0 correction		Without B_0 correction	
ROI	CW	CCW	CW	CCW
Phantom	0.15 (0.01)	0.15 (0.02)	0.29 (0.14)	0.32 (0.15)
Volunteer 1	0.42 (0.08)	0.51 (0.08)	0.48 (0.11)	0.51 (0.12)
Volunteer 2	0.37 (0.06)	0.36 (0.06)	0.43 (0.10)	0.44 (0.10)
Volunteer 3	0.35 (0.05)	0.34 (0.05)	0.44 (0.10)	0.49 (0.10)

Note: All paired *t*-tests had $p \ll 0.001$ except Volunteer 1 CCW ($p = 0.51$). Abbreviations: CW, clockwise; CCW, counterclockwise; ROI, region of interest; SD, standard deviation.

Table 3.2: Effects of B_0 compensation on mean normalized root mean square error (nRMSE) for the CIRS phantom versus gantry rotation direction

There are two chief disadvantages of B_0 compensation using the FID navigator: (1) decreased SNR, and (2) decreased imaging duty cycle. In principle, a magnetization restoration pulse can be added after the FID navigator acquisition to enhance SNR. Alternatively, the bSSFP sequence can be modified to add or redirect one of the readouts for use as a B_0 navigator while preserving the bSSFP. We used a nonselective excitation to maximize the SNR of the FID and the precision of the center frequency offset measurement due to the challenges of the low magnetic field (0.35 T).

Second, the addition of the FID navigator slightly reduces the image acquisition duty cycle. We are currently acquiring one FID navigator per k-space acquisition (frame) resulting in a 3% drop in acquisition duty cycle for the Cartesian acquisitions.

An alternative to the FID navigator is to change the transmitter and receiver frequencies in real time based on the gantry's position and velocity. The pulse sequence architecture of the ViewRay MRI–Linac permits dynamic updates to the transmitter and receiver phases and the first-order (gradient) shims.[41] Currently, the MRI–Linac sends each step-and-shoot gantry position from the motion controller to the pulse sequence over a user datagram protocol (UDP) interface to enable B_0 and first-order shim corrections while the gantry is stationary.[41] The B_0 and gradient shim corrections were based on a lookup table derived from spherical phantom measurements of off-resonance and field homogeneities performed with a stationary gantry. In principle, the UDP interface could be used to communicate the real-time gantry position and velocity back to the pulse sequence.

However, differences in center frequency were observed between the CIRS phantom and in vivo during gantry rotation. Therefore, a lookup table or model-based solution for minimizing off-resonance during rotating gantry may be unsatisfactory unless the corrected center frequency offset can be maintained within ±1/(4*TR).[22] Fortunately, the maximum variation between measured offsets was 102 Hz, which is less than 1/(4*TR) (i.e., 115 Hz).

A more complicated alternative to the FID navigator is to integrate an NMR field probe or field camera into the system architecture.[57–59] The benefit of the field camera is that it can acquire data at a high sampling rate and measure both center frequency offsets and field inhomogeneities. Dynamic field correction could combine first-order (gradient) shimming with the real-time center frequency compensation.[42,60] The MRIdian does not have second-order or higher room-temperature shim coils. Nevertheless, high-order shim drivers typically require significant settling times and, thus, would not be suitable for real-time shimming without preemphasis. However, such a field camera requires separate transmitter and receiver electronics and must be electromagnetically decoupled from the MRI and Linac. The center frequency and shim data can be fed back to the MRI pulse sequence using the UDP interface.

Uncorrected B_0 offsets during readout gradients can cause imaging isocenter shifts depending on the receiver bandwidth. Based on our measurements, uncorrected B_0 offsets from gantry rotation combined with the typical 2D bSSFP cine sequences used for treatment (rBW > 850 Hz/pixel) will result in imaging isocenter shifts of <2 mm, whereas deep respiration (55 mm displacements) along the readout direction can produce localized frequency offsets of >20 kHz. For sequences (e.g., T_1 or T_2 weighted) with receiver bandwidths comparable to the B_0 offsets, the imaging isocenter shifts may exceed the limits for radiation therapy (2 mm) or stereotactic radiosurgery (1 mm).[17]

Translating the FID navigator technique to the ViewRay MRIdian's Cartesian bSSFP cine sequences is straightforward. The main difference between our bSSFP acquisition and the MRIdian's nominal single-slice 4 frames per second (fps) and three-slice 2 fps Cartesian cines is the MRIdian uses short-term averaging (N = 2). If averaging is desired, long-term averaging is required for the FID navigator to ensure the B_0 compensation is performed once per k-space dataset.

The center superior–anterior coil element was chosen as the FID navigator signal source for this study based on: (1) its higher SNR and less dephasing (e.g., due to increased field inhomogeneity) compared to the lateral coil elements; (2) similarity of results compared to body coil reception; (3) closer proximity to the body (e.g., the posterior coil is often further away from the body due to the presence of alpha cradle); and (3) minimal processing time (e.g., 1 FID vs. 12 FIDs plus averaging). However, we subsequently found during post-processing that the average frequency offset from the total of 12 coil elements yields a frequency offset similar to the single channel result (RMSEs of <11 Hz in CIRS phantom and <24-Hz in vivo). The MRIdian A3i has a faster reconstruction engine that would minimize the FID processing time if averaging is used. In principle, one could select and process the coil elements closest to the tracking target for B_0 compensation to minimize signal dephasing near the target.

Translating the FID navigator technique to radial bSSFP acquisitions is challenging due to the long k-space acquisition window (0.5 s) and the use of view sharing. On diagnostic MRIs, eddy currents were previously calculated from, and corrections were applied to, the radial k-space spokes.[35] It is also possible to repurpose k-space spokes to serve as an FID navigator or add navigator spokes.[61]

As previously mentioned, distinguishing center frequency offsets from respiratory motion using a selective navigator with a readout gradient may be challenging because sagittal cines have the readout parallel to the principal direction of motion. Changing the readout taxis of the navigator may still result in motion-related frequency offsets on the order of kHz.[62]

The B_0 compensation described herein does not address changes in field homogeneity due to the rotating gantry. Like center frequency offsets, field inhomogeneities can cause spatial shifts in the slice-selection or readout direction, and variations in image intensity due to signal dephasing during the 2D bSSFP acquisition.[63] Field inhomogeneities can also cause geometric distortion. Based on our previous measurements of field inhomogeneities, geometric distortion and spatial shifts should have a small effect on tracking (e.g., Dice coefficient).[22,41] However, variations in image intensity due to signal dephasing from either center frequency offsets or field inhomogeneities can affect tracking. We prioritized center frequency offsets (800 Hz range) over field inhomogeneities (160 Hz FWHM) in this study.

3.5 Conclusions

Center frequency offsets induced by the rotation of the ferromagnetic gantry resulted in image quality degradation while using bSSFP cine sequences in a 0.35 T MRI-Linac. Dynamic B_0 compensation using an FID navigator improved image quality and reduced null band artifacts albeit with a small drop in acquisition duty cycle and SNR. Future work is warranted to minimize the effects of the B_0 compensation on duty cycle and SNR.

Chapter 4: Minimizing CIED Artifacts on a 0.35 T MRI-Linac Using Deep Learning

4.1 Introduction

MRI guided radiotherapy (MRgRT) provides real-time target tracking and superior soft tissue contrast compared with conventional CBCT systems.[9–12] Cine images are appealing because they can be acquired continuously at high frame rates during treatment because MRI is nonionizing. The high duty cycle cine MRIs facilitate target gating based on the underlying anatomy as opposed to a motion surrogate that may become decorrelated with target motion during prolonged treatment.

Noninvasive cardiac radioablation (CRA) is a recently developed approach for patients presenting with ventricular tachycardia (VT) refractory to standard drug and catheter ablation therapy.[23,24] CRA is typically performed using cone-beam CT image guided radiotherapy (CBCT-IGRT) to deliver 25 Gy in a single fraction to the myocardial lesion that produces the arrythmia. There is limited experience using MRgRT to treat the heart with radiation.[64,65] Currently, the treatment target needs to be expanded by 7-10 mm to account for motion, gating uncertainties inherent to CBCT-IGRT, and patient setup.[24] These margin expansions result in healthy tissue volumes around the true target receiving therapeutic dose to ensure complete target coverage. Target margins and radiotoxicities could potentially be reduced by adopting an MRgRT over a CBCT-IGRT approach. MRgRT enables continuous MRI at high frame rates throughout treatment. The treatment beam can be gated to only allow for treatment during specific cardiac and respiratory phases without relying on surrogate signals.

Balanced steady state free procession (bSSFP) cine sequences are currently used for real-time imaging during MRgRT treatment. bSSFP sequences offer high temporal resolution and signal-to-noise ratios (SNR) but are prone to imaging artifacts from intravoxel dephasing.[48] Unfortunately, the cardiac implantable electronic device (CIED) pulse generator commonly found in VT patients cause large magnetic susceptibility artifacts due to ferromagnetic components. The artifacts from the nonferrous leads are minor in comparison.

The proximity of the implanted CIEDs to the heart can result in unsatisfactory image quality for most cardiac radiosurgery applications. In CT and CBCT, streaking artifacts resulting from the CIED pulse generator and leads interfere with delineation of the target scar even if metal artifact reduction is used. bSFFP artifacts include both signal dephasing near the CIED and null bands emanating from the device into the heart.[65] Alternative MRI cine sequences, such as fast gradient-echo sequences, that reduce artifacts may sacrifice SNR, temporal resolution, or spatial resolution and fidelity.[66,67]

In this study, we explore a post-processing solution to reduce CIED-related artifacts. Several machine learning (ML) techniques were developed for image-to-image translation and artifact reduction. Generative adversarial networks (GANs) were successful for MRI reconstruction, denoising, super-resolution, segmentation, motion artifact reduction, and image modality translation.[67–75] However, an unsupervised learning approach is often required due to the difficulty in acquired paired image data or generating physiologically meaningful synthetic datasets. Cycle-consistent generative adversarial network, or CycleGAN, is a widely used unsupervised deep learning architecture for image-to-image translation problems.[76] CycleGAN was reported to be successful in several clinically relevant domains including CT metal artifact reduction, visual enhancement of CBCT images, and synthetic CT generation.[77–80] This study investigates using CycleGAN to reduce CIED artifacts in bSSFP MRI cines for use in CRA.

4.2 Materials and Methods

4.2.1 Theory

The CycleGAN architecture utilizes two generators and two discriminators to translate images from one source domain to another without pairing images between the two domains.[76] Images from domain X are transformed to domain Y by training one generator to learn the mapping G: X -> Y and the other to learn the mapping F: Y -> X. The network architecture is shown in Figure 4.1 with the Y domain corresponding to images with CIED artifacts and the X domain corresponding to images without CIED artifacts.

The adversarial objective functions for generators G and F and discriminators D_y and D_x are given by:

$$\min_{G} Loss_G(G) = E_{x \sim p_{data}(x)}\left[D_y\big(G(x)\big) - 1\right]^2 \qquad (4.1)$$

$$\min_{D_y} Loss_{D_y}(D_y) = E_{y\sim p_{data}(y)}[D_y(y) - 1]^2 + E_{x\sim p_{data}(x)}\left[D_y(G(x))^2\right] \quad (4.2)$$

$$\min_{F} Loss_F(F) = E_{y\sim p_{data}(y)}[D_x(F(y)) - 1]^2 \quad (4.3)$$

$$\min_{D_x} Loss_{D_x}(D_x) = E_{x\sim p_{data}(x)}[D_x(x) - 1]^2 + E_{y\sim p_{data}(y)}\left[D_x(F(y))^2\right] \quad (4.4)$$

Where $x \in X$, $y \in Y$, and p_{data} is the data manifold to be learned. Minimizing these objective functions is equivalent to minimizing the Pearson χ^2 divergence.[81] These adversarial losses originated from the LS-GAN architecture and were shown to decrease the vanishing gradient problem compared to cross-entry loss functions in GANs.[81]

The cycle consistency loss reduces the space of possible mapping functions and ensures the model retains consistency when mapping output images back to their initial domain. This loss can be broken down into a forward loss ($F(G(x)) \approx x$) and a backward loss ($G(F(y)) \approx y$). The full cycle consistency loss can be written as:

$$Loss_{\mathrm{cycle}}(G,F) = \lambda_{\mathrm{x}}\, \mathrm{E}_{\mathrm{x}\sim \mathrm{p_{data}(x)}}\left[\left\|\mathrm{F}(\mathrm{G}(\mathrm{x})) - \mathrm{x}\right\|_1\right] + \lambda_{\mathrm{y}}\, \mathrm{E}_{\mathrm{y}\sim \mathrm{p_{data}(y)}}\left[\left\|\mathrm{G}(\mathrm{F}(\mathrm{y})) - \mathrm{y}\right\|_1\right] \quad (4.5)$$

where λ_x and λ_y are weights that control the emphasis placed on either the forward or backwards loss.

To preserve content, an additional identity loss can be added to the overall objective function that maintains that $G(y) \approx y$ and $F(x) \approx x$. This loss has the effect of making the model more conservative when encountering unknown content, preserving color in the case of RGB inputs, and discouraging the network from making large changes to inputs that already appear similar to images in the target domain. The identity loss is given by the following:

$$Loss_{identity}(G,F) = \lambda_x\, E_{x\sim p_{data}(x)}[\|F(x) - x\|_1] \,+\, \lambda_{identity}\Big[\lambda_y\, E_{y\sim p_{data}(y)}\big[\big\|G(y)\big) - y\|_1\big]\Big]$$

(4.6)

where $\lambda_{\text{identity}}$ acts to scale the identity loss relative to the other loss functions.

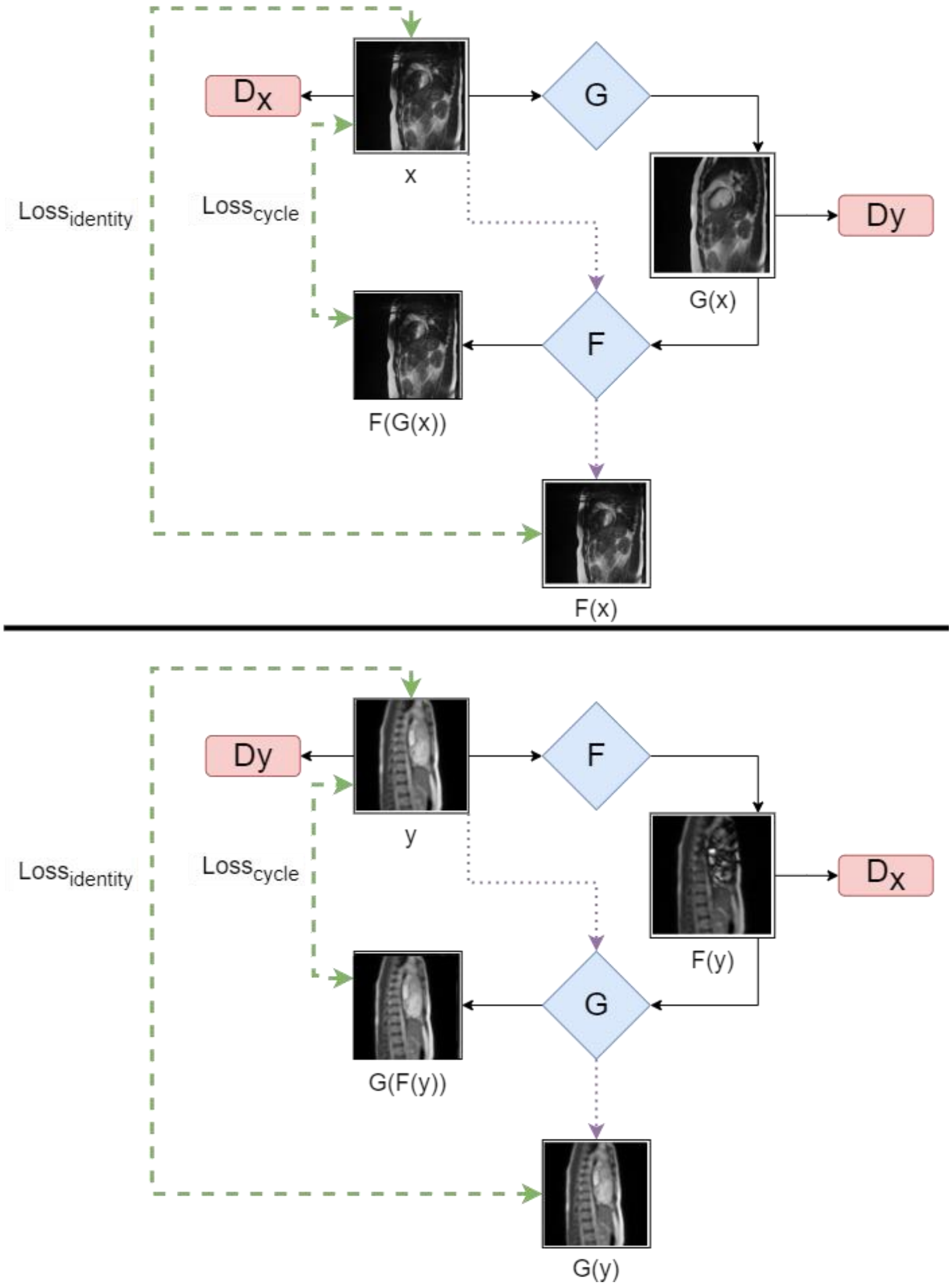

Figure 4.1 CycleGAN architecture shown as two flow charts. F and G are generator networks (shown in blue) where F maps from domain Y to domain X, and G maps from domain X to domain Y. D_x and D_y are discriminator networks (shown in red) that are trained to return a 0 for images not in the target domain (X for D_x and Y for D_y) and return 1 for images in the target domain. The identity and cycle loss inputs are indicated

by a green dashed arrow. The identity loss image generation is shown via the purple dotted arrows. (Top) The pathway for an image, x, in domain X. X in this case corresponds to the domain containing CIED artifacts. (Bottom) The pathway for an image, y, in domain Y. Y corresponds to the image domain without artifacts.

4.2.2. Data Acquisition

Fourteen healthy volunteers (eight males and six females, ages 22 to 74 with mean age of 42.4 ± 16.6 years old, and weights 60-106 kg with a mean weight of 76.85 ± 11.61 kg) were selected in accordance with an Institutional Review Board approved protocol to be imaged on 0.35 T MRgRT system (ViewRay MRIdian®, Oakwood Village, OH). All scans were performed using the MRI subsystem (Siemens IDEA/ICE version VB19) in “MRI QA” mode using two (posterior and anterior) flexible six-channel torso coils. Volunteers were positioned head-first supine with the coils positioned for thoracic imaging. Scans were performed with the volunteer’s arms at their sides to increase comfort.

Images were acquired using a 2D sagittal cartesian 4 frames/s (fps) bSSFP cine sequence (TR: 2.1 ms, TE: 0.91 ms, GRAPPA: 2, Partial Fourier: 5/8, Pixel Bandwidth: 1351 Hz/pixel, Matrix: 100x100, Field of View: 350 mm, 2 averages). Volunteers were imaged with an MR Conditional implantable cardiac defibrillator (ICD, Medtronic Visia AF MRI SureScan Model DVFB1D1, Minneapolis, MN) securely taped to their upper left pectoral region with leads (Models 6944-75 and Sprint Quattro DF-1/IS-1) running toward the ventricles to simulate an implanted ICD. Scans were then repeated immediately after removing the ICD. The resulting DICOM images were aggregated into a domain with the CIED artifact and a domain without artifact. The images from the last two volunteers scanned (Volunteer 13 and Volunteer 14) were separated as testing data while the other twelve volunteer datasets were used for training. This resulted in 18,149 artifact-free training images, 19,758 CIED artifact training images, 1,000 artifact-free testing images, and 1,000 CIED artifact testing images. The model was then retrained three separate times using the datasets from a randomly chosen volunteer as the testing data (Volunteer 8, Volunteer 3, and Volunteer 11) for evaluation.

4.2.3. Data Analysis

CycleGAN training was performed using Pytorch and Python version 3.7 for 50 epochs (48 hours). The weight for the identity loss ($\lambda_{identity}$) was set at 0.7 to ensure that the resulting output images emphasized retaining content from the input image. The forward and backward cycle consistency loss weights (λ_x and λ_y) were set at 10. All DICOM images were up-scaled to a size of 256x256 pixels using bicubic interpolation. The two generators used a 9-block ResNet architecture while the two discriminators used a 70x70 PatchGAN architecture.[82]

All image analysis was performed in MATLAB version 2022a. The 1,000 test images without artifacts were paired with the 1,000 test images with CIED artifacts by calculating the multiscale structural similarity (MS-SSIM) index for each possible pair of images and selecting the highest scoring pair.[83] The paired test images without artifacts were treated as reference images for comparison with the CycleGAN reconstructed test images.

To assess target tracking, a reference contour of the whole heart was drawn on the fifth artifact-free test image for both volunteers in the artifact-free test dataset. The fifth image was chosen over the first image in each dataset to ensure that bSSFP sequence had reached steady state. Contours were then generated on each test image using an active contour algorithm described by Chan et al.[55] Dice coefficients were calculated for the CycleGAN reconstructed image contours and the CIED artifact test images contours using the contours created on the paired artifact free test images as the ground truth.

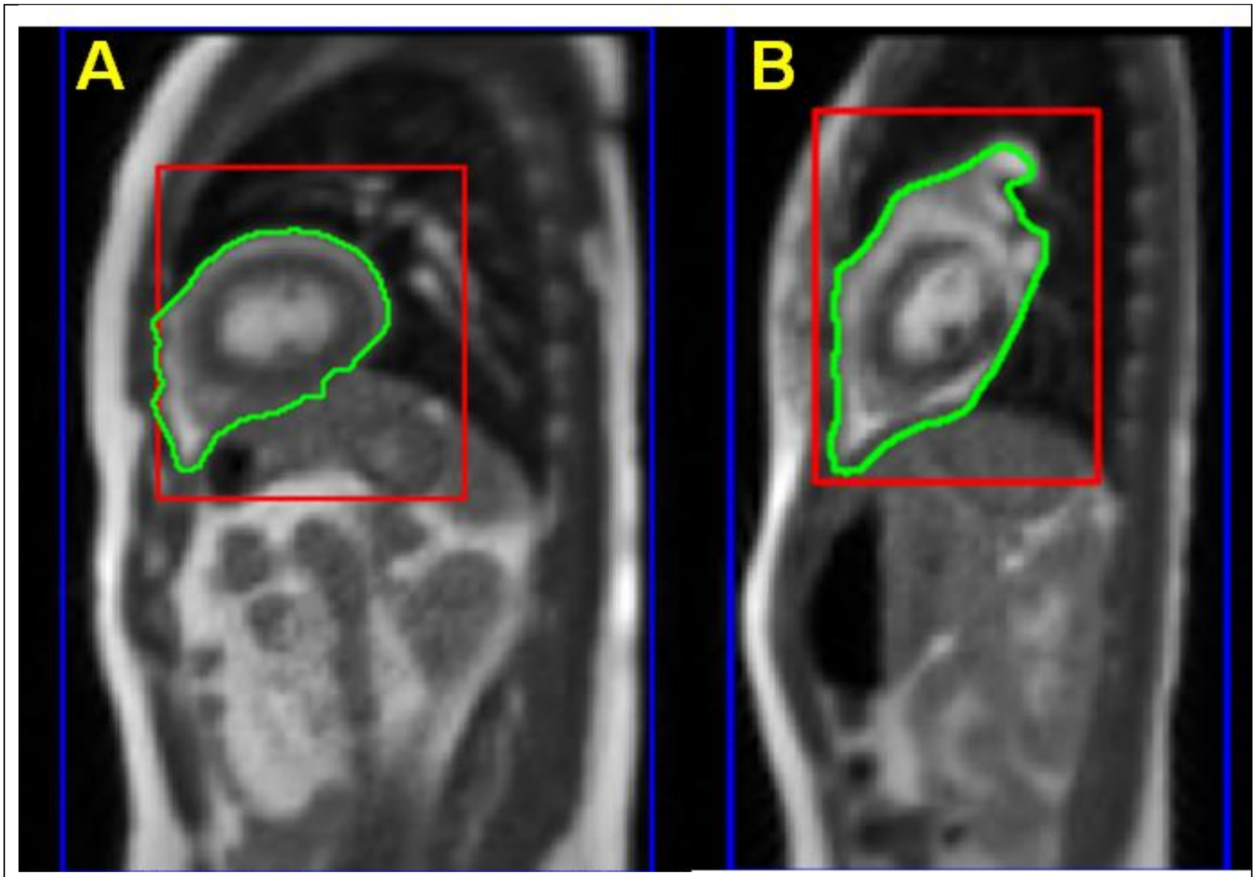

Figure 4.2: Regions of interest (ROIs) for the test images from Volunteer 13 (A, 30-year old male) and Volunteer 14 (B, 31-year old female). Blue corresponds to the body ROI. Red corresponds to the heart and nearby tissue ROI. Green is the heart contour generated from the active contouring algorithm.

Image quality was scored by calculating the peak signal to noise ratio (PSNR), normalized root mean squared errors (NRMSE), and MS-SSIM score for the CycleGAN reconstructed images and the CIED artifact test images. Image quality metrics were calculated over three different regions of interest (ROIs): the region corresponding to the contour on the paired reference image, a larger rectangular region that includes the area surrounding the heart, and a rectangular region that includes the body to reduce the influence of noise outside of body on the results. An example of the different ROIs is shown in Figure 4.2. Paired t-tests were performed for all image quality metrics and Dice coefficients to assess significance.

The trained CycleGAN model was tested on three additional 4 fps bSSFP cine MRI datasets acquired in 2018. The first dataset was acquired in a 61-year-old male VT patient with an implanted MR Conditional ICD (Medtronic Evera MRI Surescan Model DDMC3D4) and leads (Model 5076 CapSureFix Novus and Model 6935 Sprint Quattro Secure S) treated on the 0.35 T MRI-Linac.[65] The other two test cases were acquired with the same CIED and external placement as the other 14 volunteers. The second cine MRI dataset was acquired from a 28-year-old male acquired on the 0.35 T MRI-Linac. The third MRI dataset was acquired from a 38-year-old male volunteer scanned on a ViewRay MRI-Cobalt-60 radiotherapy system ramped to 0.32 T. Because none of these cine MRIs were acquired with an CIED-free reference set of images, the CycleGAN generated images were compared qualitatively.

4.3 Results

Figure 4.3 shows an example of the artifact reduction and tracking improvement using the trained CycleGAN model for Volunteer 13 (30-year old male) and Volunteer 14 (31-year old female). The susceptibility artifact from the CIED was substantially reduced for the CycleGAN reconstructed images. Image content not affected by the CIED was largely retained after using CycleGAN to reduce CIED artifacts.

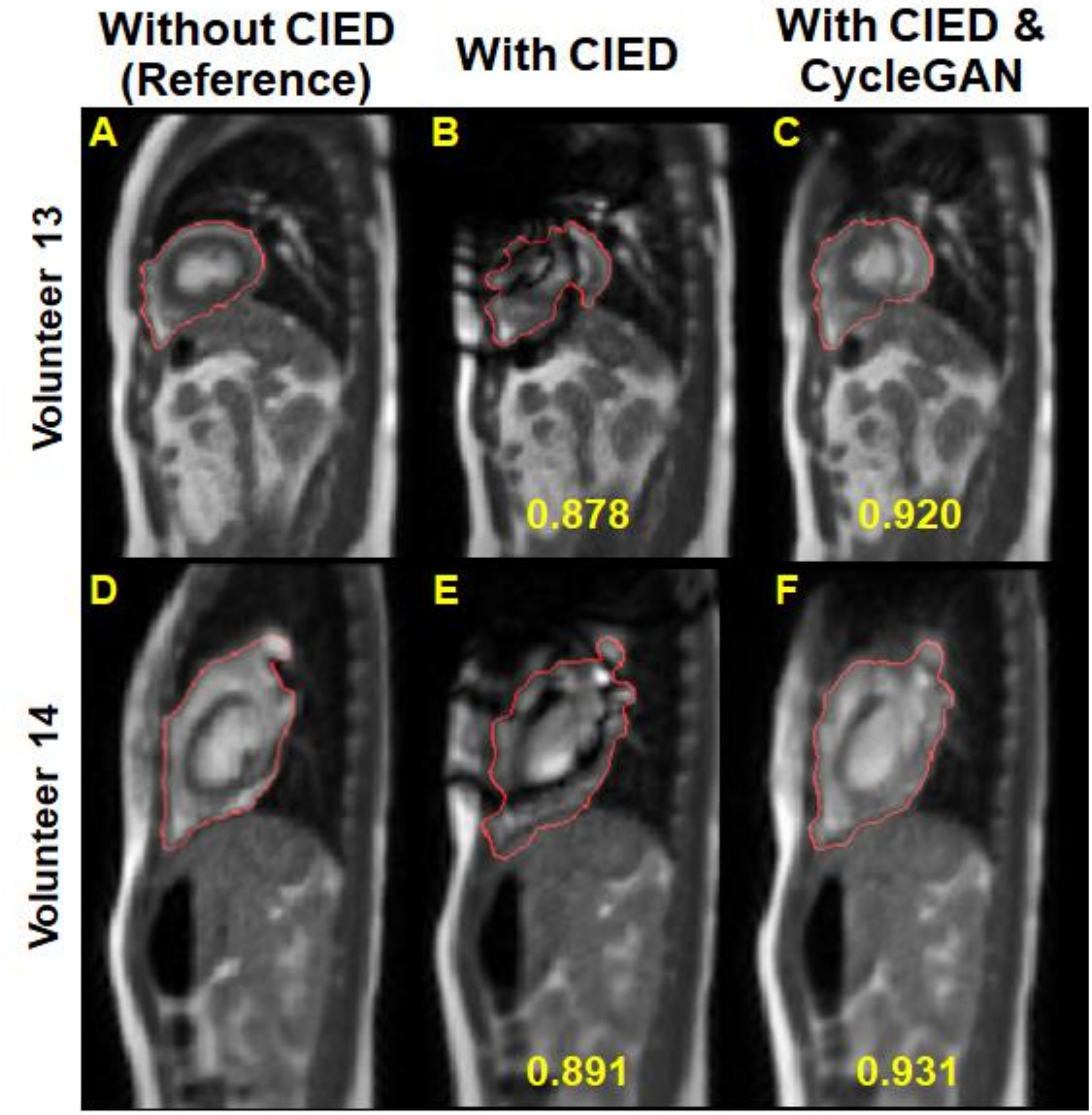

Figure 4.3: Images and tracking contours from Volunteer 13 (A-C) and Volunteer 14 (D-F). Dice coefficients are shown in yellow at the bottom of the images acquired with the CIED present. The CycleGAN generated images (C, F) resulted in a sharp reduction in susceptibility artifacts and higher Dice coefficients to enable better tracking.

Mean Dice coefficients over all the testing images improved from 0.910 ± 0.017 to 0.932 ± 0.015. Mean image quality metrics, averaged over each image, are presented in

Table 4.1 for each volunteer using in testing and all ROIs. All paired t-tests had $p<<0.001$ indicating a significant benefit in the CycleGAN generated images compared with the untouched CIED images. The CycleGAN reconstructed images showed an increase in tracking performance via Dice coefficient, MS-SSIM, and PSNR while also reducing the nRMSE. Histograms for the Dice coefficients and image quality metrics for the full body ROI are presented in Figure 4.4 for Volunteer 13 and Volunteer 14.

TABLE 4.1 Mean image quality metrics for MRIs with the CIED present without (labeled "CIED Artifact") and with CycleGAN reconstruction.

Volunteer 13

	Heart Contour		ROI Heart+Surrounding Tissue		ROI Full Body	
	CIED Artifact	CycleGAN	CIED Artifact	CycleGAN	CIED Artifact	CycleGAN
nRMSE	2.573 ± 0.297	1.281 ± 0.155	1.469 ± 0.151	0.923 ± 0.085	0.585 ± 0.084	0.366 ± 0.022
MS-SSIM	0.958 ± 0.008	0.987 ± 0.002	0.893 ± 0.014	0.953 ± 0.005	0.786 ± 0.027	0.848 ± 0.011
PSNR	26.875 ± 1.262	32.927 ± 0.971	24.837 ± 1.052	28.856 ± 0.612	18.140 ± 1.176	22.148 ± 0.485

Volunteer 14

	Heart Contour		ROI Heart+Surrounding Tissue		ROI Full Body	
	CIED Artifact	CycleGAN	CIED Artifact	CycleGAN	CIED Artifact	CycleGAN
nRMSE	1.950 ± 0.112	1.136 ± 0.122	1.471 ± 0.075	0.952 ± 0.069	0.607 ± 0.032	0.509 ± 0.023
MS-SSIM	0.947 ± 0.008	0.980 ± 0.004	0.908 ± 0.006	0.951 ± 0.005	0.811 ± 0.009	0.843 ± 0.007
PSNR	25.403 ± 0.549	30.137 ± 0.907	23.607 ± 0.417	27.398 ± 0.567	20.890 ± 0.452	22.421 ± 0.332

Volunteer 8

	Heart Contour		ROI Heart+Surrounding Tissue		ROI Full Body	
	CIED Artifact	CycleGAN	CIED Artifact	CycleGAN	CIED Artifact	CycleGAN
nRMSE	2.016 ± 0.240	1.042 ± 0.105	1.614 ± 0.176	0.834 ± 0.073	0.622 ± 0.110	0.437 ± 0.025
MS-SSIM	0.931 ± 0.016	0.974 ± 0.004	0.881 ± 0.019	0.954 ± 0.005	0.779 ± 0.037	0.790 ± 0.012
PSNR	23.872 ± 1.020	29.586 ± 0.962	22.311 ± 0.935	28.022 ± 0.859	18.555 ± 1.470	21.496 ± 0.426

Volunteer 3

	Heart Contour		ROI Heart+Surrounding Tissue		ROI Full Body	
	CIED Artifact	CycleGAN	CIED Artifact	CycleGAN	CIED Artifact	CycleGAN
nRMSE	1.349 ± 0.169	0.550 ± 0.099	1.197 ± 0.157	0.513 ± 0.079	0.464 ± 0.092	0.277 ± 0.025
MS-SSIM	0.948 ± 0.010	0.983 ± 0.004	0.935 ± 0.013	0.974 ± 0.005	0.861 ± 0.026	0.897 ± 0.011
PSNR	24.389 ± 0.922	32.245 ± 1.609	23.333 ± 0.988	30.722 ± 1.335	19.452 ± 1.544	23.786 ± 0.771

Volunteer 11

	Heart Contour		ROI Heart+Surrounding Tissue		ROI Full Body	
	CIED Artifact	**CycleGAN**	**CIED Artifact**	**CycleGAN**	**CIED Artifact**	**CycleGAN**
nRMSE	0.147 ± 0.154	1.037 ± 0.165	2.689 ± 0.199	1.425 ± 0.219	0.943 ± 0.095	0.511 ± 0.044
MS-SSIM	0.863 ± 0.024	0.950 ± 0.011	0.831 ± 0.025	0.935 ± 0.009	0.660 ± 0.036	0.717 ± 0.015
PSNR	18.796 ± 0.578	25.203 ± 1.348	20.057 ± 0.560	25.647 ± 1.236	16.681 ± 0.764	21.987 ± 0.780

CycleGAN artifact-reduced images from the three cine MRI datasets without a CIED reference are shown in Figure 4.5. All three show a reduction in banding artifacts near the heart although the images from the volunteer scanned on the 0.32 T MRI-Cobalt-60 radiotherapy system results are unsatisfactory.

Results from the retrained test datasets for randomly chosen Volunteer 3 (74-year old female), Volunteer 8 (30-year old male), and Volunteer 11 (58-year old male) are shown in Figures 4.6 and 4.7. For each randomly chosen test dataset, the model was retrained using the other (complementary) 13 volunteer datasets.

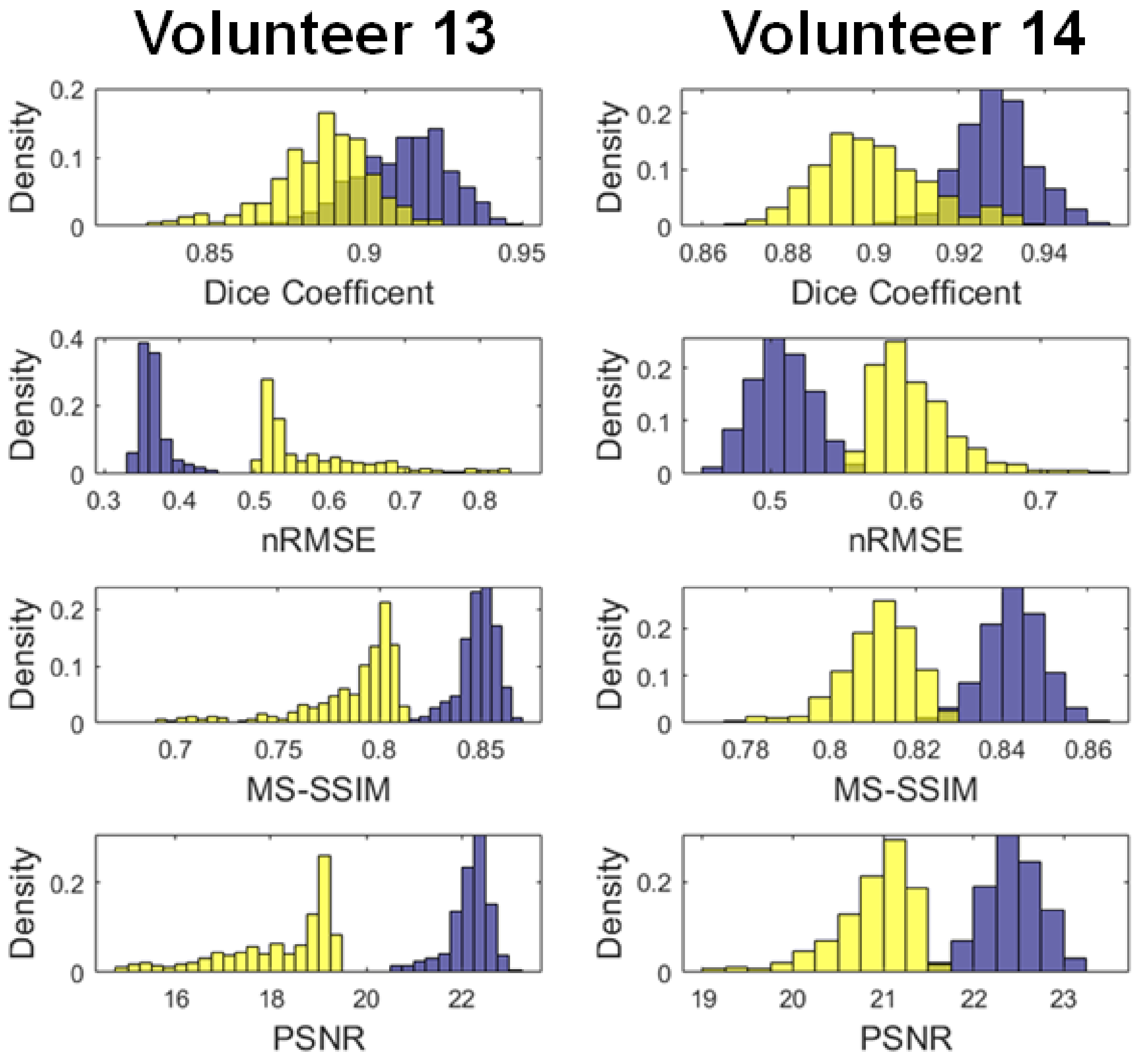

Figure 4.4: Histograms for the CIED artifact images (yellow) and images using CycleGAN artifact reduction (purple) for both volunteer datasets used for testing. Image quality metrics were measured over the full body ROI.

4.4 Discussion

The objective of this work was to investigate using CycleGAN to reduce CIED susceptibility artifacts in bSSFP cines commonly used in MRgRT. The trained CycleGAN model increased Dice coefficients and potentially tracking performance of the whole heart. The CycleGAN also improved image quality with the CIED present as indicated by the reduction in nRMSE and improvements in both PNSR and MS-SSIM.

The main limitation of this study is the small sample size (i.e., number of data sets). Additional training data should further improve the CycleGAN artifact reduction capabilities. Since the training data comes from only 12 volunteers, the training data had a high degree of correlation between training images.

One additional limitation of this study is that the test image pairs used to evaluate performance were imperfect. The test image pairing based on MS-SSIM scores resulted in data pairs that visually tracked the cardiac and respiratory cycle well. However, small differences in the lung vasculature and abdominal structures remained in place due to slight differences in image positioning, coil placement, and physiological motion. While great care was taken to keep the volunteers and receiver coils from moving when removing the CIED, deviations between the data acquired with the CIED present and absent are likely. Generating high quality, realistic, synthetic susceptibility artifacts on digital, anatomically correct MRI phantoms could provide a more robust data source.

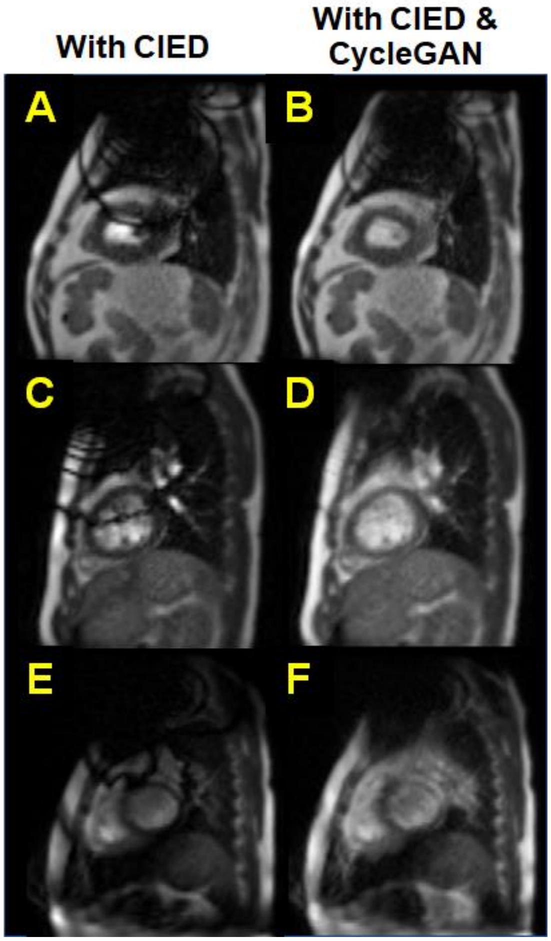

Figure 4.5 Application of CycleGAN to the three CIED datasets not used in model training or testing. Sagittal 4 fps cine bSSFP MRIs are shown without (A, C, E) and with (B, D, F) CycleGAN processing. (A, B) 61-year-old male VT patient with implanted ICD. (C, D) 28-year-old and (E, F) 38-year-old healthy male volunteers. The latter (E, F) was scanned on a ViewRay MRI-Cobalt-60 MRgRT ramped to 0.32 T.

While the CycleGAN generated images are a significant improvement over the images with CIED susceptibility artifacts, they are not perfect representations of the underlying reference data. Images exhibit some blurring in and around the region where the CIED artifacts previously were positioned. The blurring may limit the tracking accuracy of smaller targets near the susceptibility artifacts.

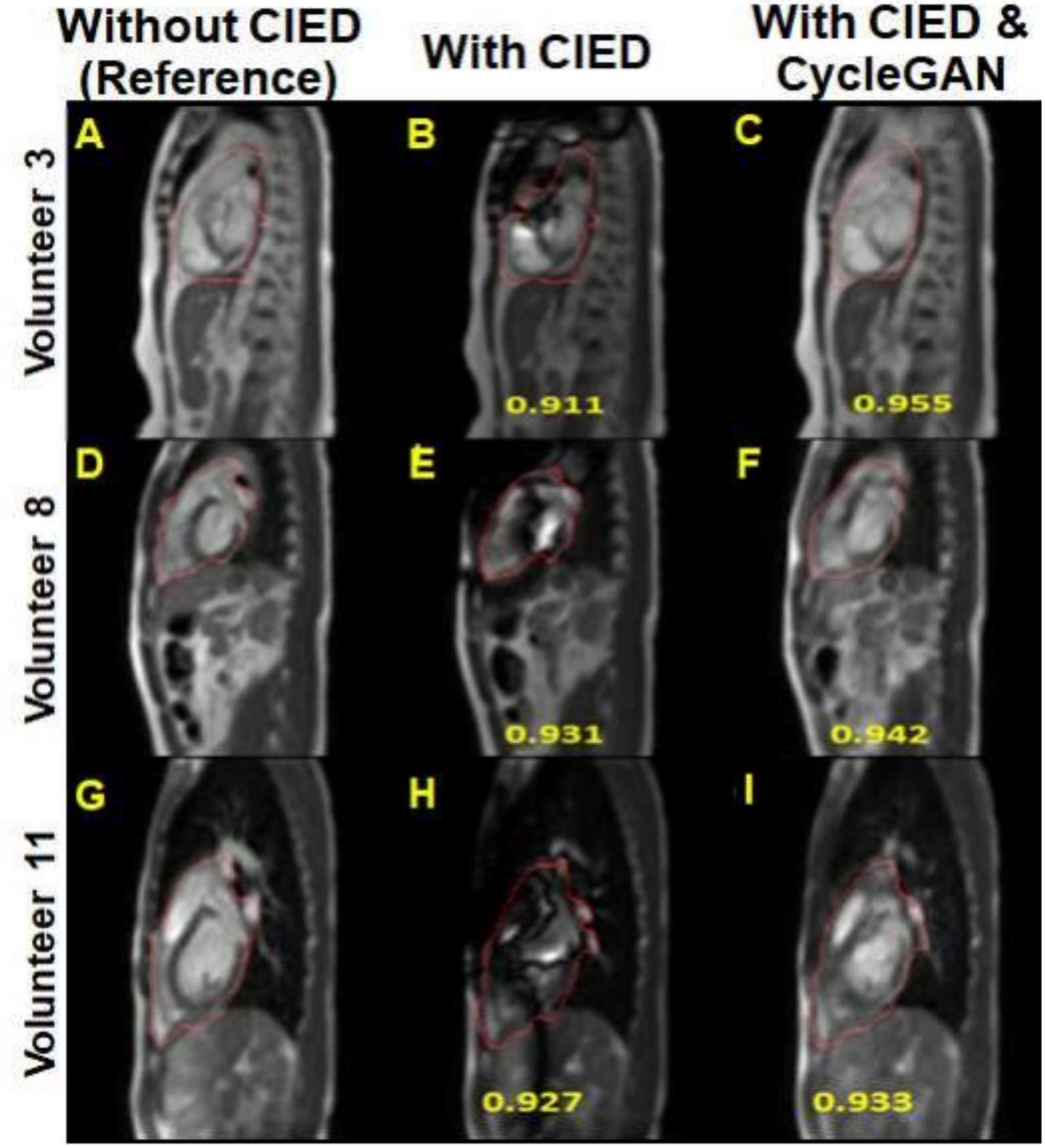

Figure 4.6: Images and tracking contours from Volunteer 3 (A-C), Volunteer 8 (D-F), and Volunteer 11 (G-I). From left: MRIs acquired without the CIED present (A, D, and G), and with the CIED present (B, E, and H) and reconstructed using the CycleGAN (C, F, and I). Dice coefficients are shown in yellow at the bottom of the images acquired with the CIED in place. The CycleGAN generated images (C, F, and I) resulted in reduced susceptibility artifacts and higher Dice coefficients.

The CycleGAN method can be applied to other cine sequences used in MRgRT (e.g., ViewRay's 8 fps radial cine sequence) if trained with the respective sequence. However, we use the 4 fps cartesian cine sequence by default for patients with metal implants since its specific absorption rate is roughly half of the 8 fps sequence and treatments may require over an hour of continuous MRI acquisition.

The implementation of GANs directly into the vendor-provided online reconstruction pipeline is challenging due to the lack of support for programming languages regularly used for machine learning (e.g., Python, MATLAB, and R). While packages like Pytorch and Tensorflow have the capability to deploy models in C++, compatibility with the vendor specific reconstruction compiler version may be cumbersome. However, open-source reconstruction frameworks with Python 3 support, such as Gadgetron, may ease the translation of these techniques into a real-time clinical environment.[84]

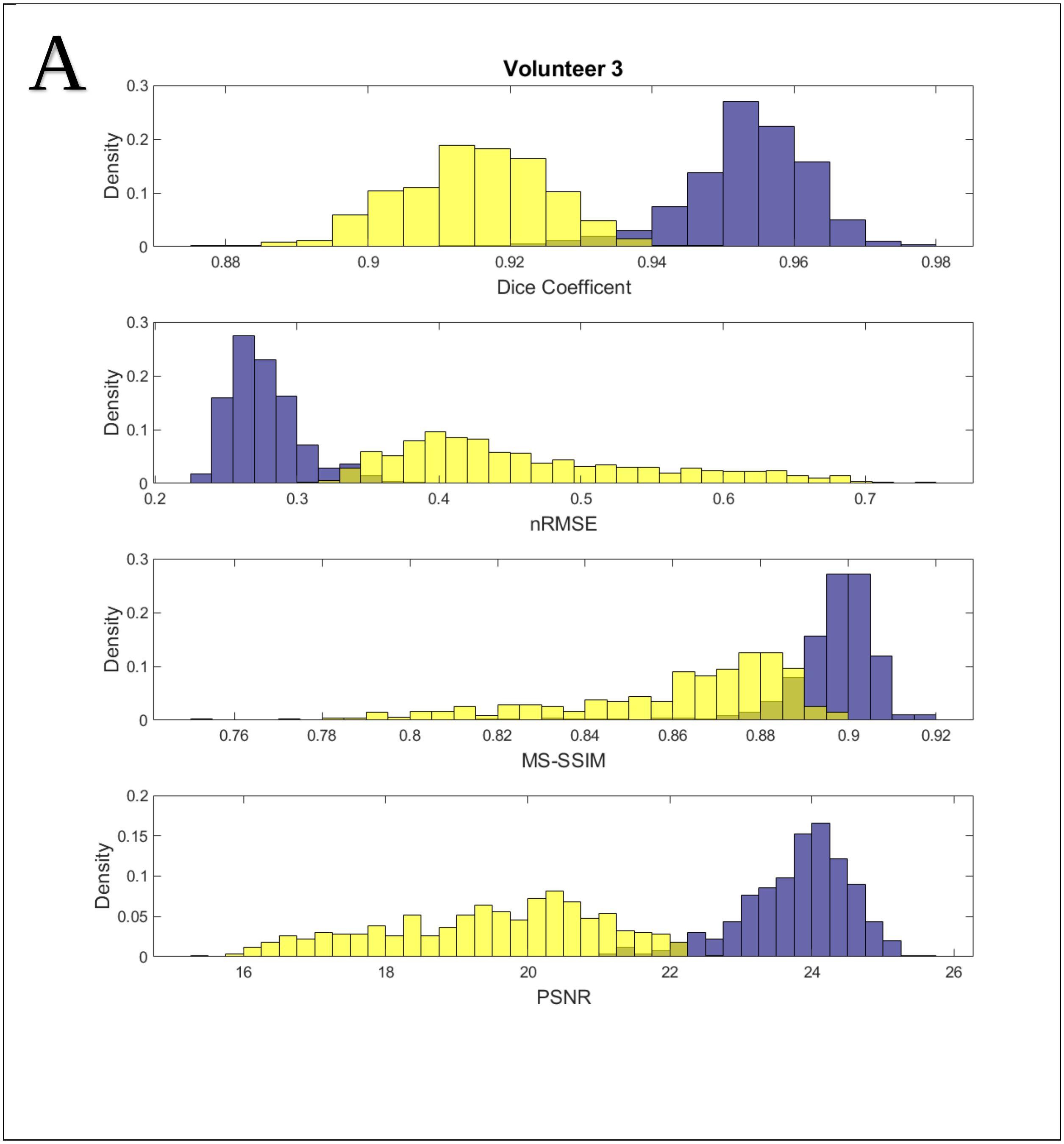
A
Volunteer 3
Density
0.3
0.2
0.1
0
0.88
0.9
0.92
0.94
0.96
0.98
Dice Coefficent
Density
0.3
0.2
0.1
0
0.2
0.3
0.4
0.5
0.6
0.7
nRMSE
Density
0.3
0.2
0.1
0
0.76
0.78
0.8
0.82
0.84
0.86
0.88
0.9
0.92
MS-SSIM
Density
0.2
0.15
0.1
0.05
0
16
18
20
22
24
26
PSNR

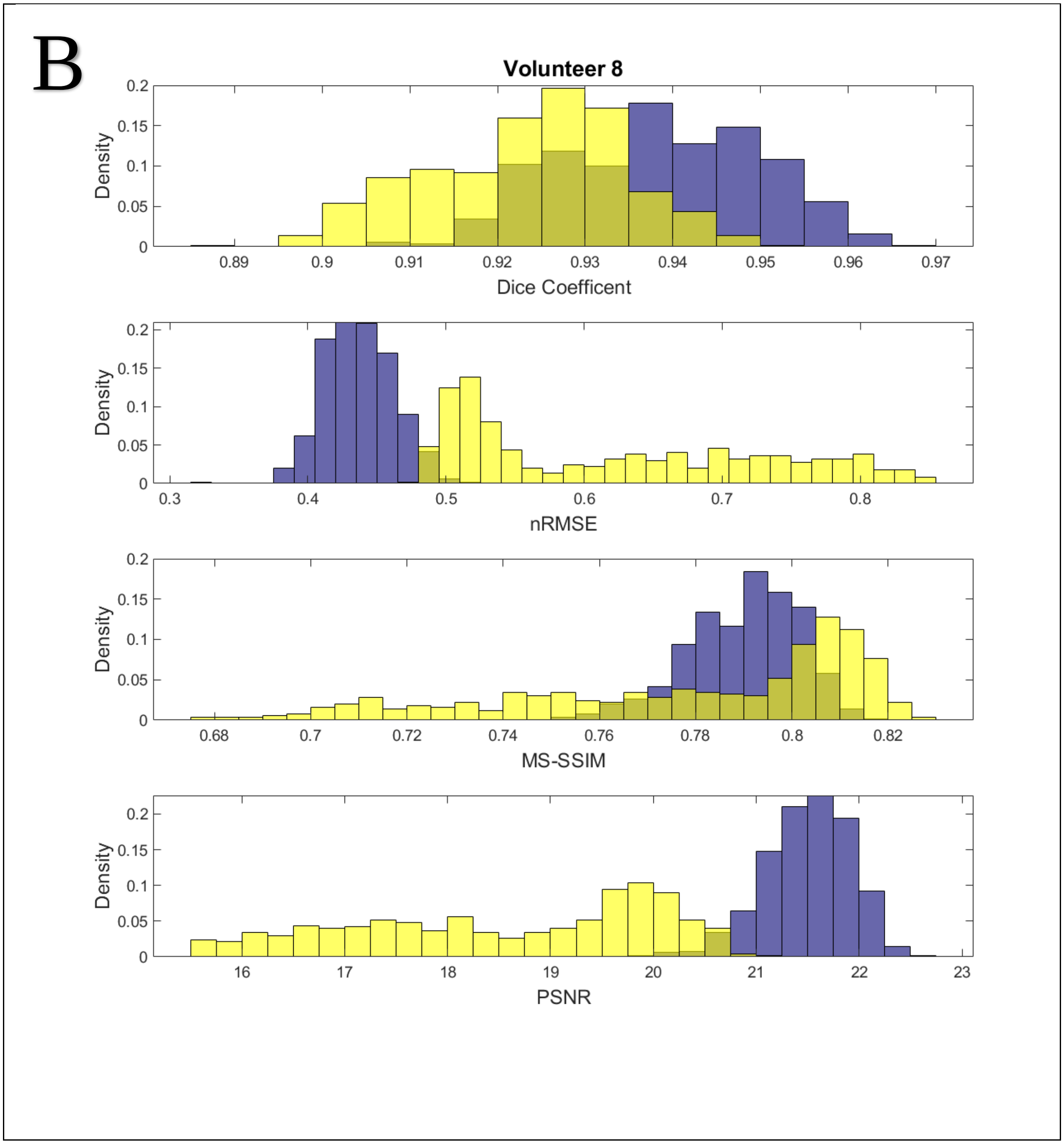
B
Volunteer 8
Density
0.2
0.15
0.1
0.05
0
0.89
0.9
0.91
0.92
0.93
0.94
0.95
0.96
0.97
Dice Coefficent
Density
0.2
0.15
0.1
0.05
0
0.3
0.4
0.5
0.6
0.7
0.8
nRMSE
Density
0.2
0.15
0.1
0.05
0
0.68
0.7
0.72
0.74
0.76
0.78
0.8
0.82
MS-SSIM
Density
0.2
0.15
0.1
0.05
0
16
17
18
19
20
21
22
23
PSNR

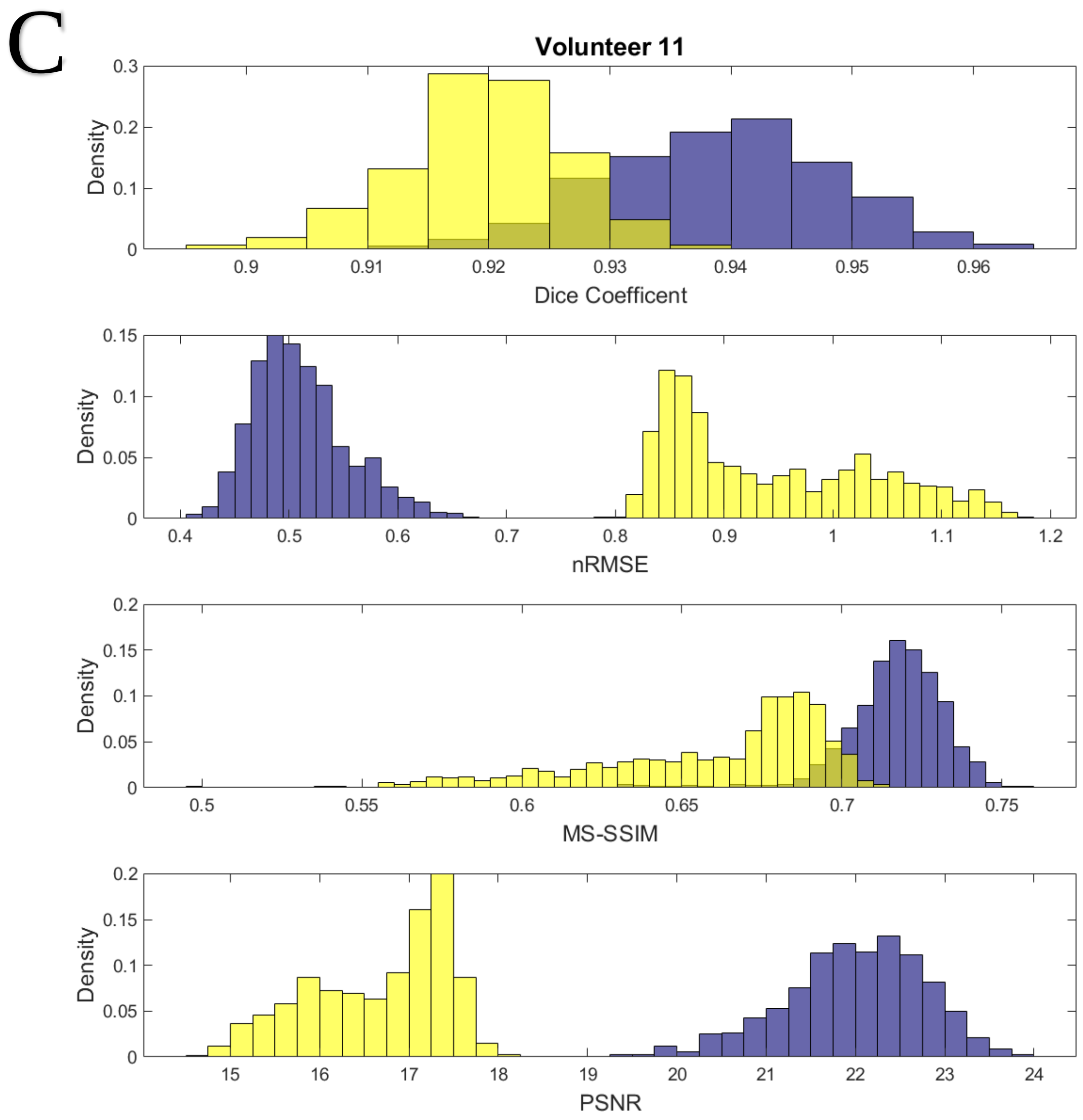

FIGURE 4.7 Histograms from the CIED artifact images (yellow) and images generated using CycleGAN artifact reduction (purple) for the randomly chosen volunteer datasets used for testing. Top row: Volunteer 3 (A) and Volunteer 8 (B). Bottom row: Volunteer 11 (C). Image quality metrics were calculated over the full body ROI. The CycleGAN reconstructed images caused an increase in the Dice similarity coefficient, peak signal-to-noise ratio (PSNR), and multiscale structural similarity (MS-SSIM) while reducing the normalized root mean square error (nRMSE).

4.5 Conclusions

CycleGAN was demonstrated to reduce susceptibility induced bSSFP artifacts caused by MR Conditional CIEDs even with limited training data. CycleGAN generated images displayed a significant improvement in image similarity for tracking of the whole heart and showed an improvement in image quality compared to the images with artifact.

Chapter 5: Conclusions and Future Directions

MRgRT is an exciting development in IGRT. However, the MRI subsystems on MRI-Linacs are inherently based on hardware and software developed for diagnostic MRIs. As the technology continues to expand, researchers and vendors will need to continue to address issues specific to MRgRT. The work presented in this dissertation serves as a foundation for overcoming some of these limitations.

The Siemens MRI subsystem on the ViewRay 0.35 T MRI-Linac has built-in software for dynamically correcting B_0 inhomogeneities and off-resonances (both first and zeroth order). However, the software correction was created for the purpose of correcting B_0 inhomogeneities in a diagnostic MRI without a rotating radiation therapy gantry.

The work in **Chapter 2** quantified first and zeroth order B_0 and gradient eddy currents before and after a hardware modification installed by the vendor to address imaging isocenter variations. While the hardware modification significantly reduced the imaging isocenter shifts, additional work is warranted to reduce gantry angle dependent B_0 eddy currents that remain outside of vendor specifications. One possible solution to this problem could be building a look-up table of eddy current corrections on the MRI subsystem at different gantry angles using triangular gradients to generate a net gradient impulse response function.[85] Another possibility could be an expansion of the existing Siemens ECC tool that permits dynamic updates based on the current gantry position into account. However, dynamic changes in shim coil currents may be vulnerable to settling times.

The work presented in **Chapter 3** uses a modified bSSFP sequence to correct for B_0 fluctuations during gantry rotation in real-time. The use of navigators in the sequence inherently reduces SNR due to disrupting the steady-state and results in a minor increase in imaging times. An alternative option to using navigators to estimate B_0 offsets would be to take a model-based approach. By modifying equation 3.3 to account directly for the gantry position over time to:

$$s(t) = \left(A \cdot \left|\frac{\dot{\theta}(t)}{\omega_{max}}\right| \cdot Sin[6(\theta(t) + B)]\right)(u[t_{start}] - u[t_{start} - t_{end}]) + C \qquad 5.1$$

the linear accelerator gantry motion controller data can be used directly to estimate B_0 fluctuations. One issue with this approach is the noise present in the gantry inclinometer. The gantry angle data was smoothed by computing the 11-point moving average to reduce the noise in the data. A symmetric low-pass differentiator with an 11-point window length was numerically convolved with the inclinometer data to calculate gantry velocity. These filters resulted in a 0.125 second delay in the gantry angle data. Figure 5.1 shows the model fit compared to the measured B_0 offsets for a complete counterclockwise rotation of the gantry using a DSV phantom doped with 5 mM $NiSO_4$ (T_1/T_2: 330/260 ms). Integrating these models and gantry angle data into the MRI subsystem remains challenging and represents a pathway for future experimentation.

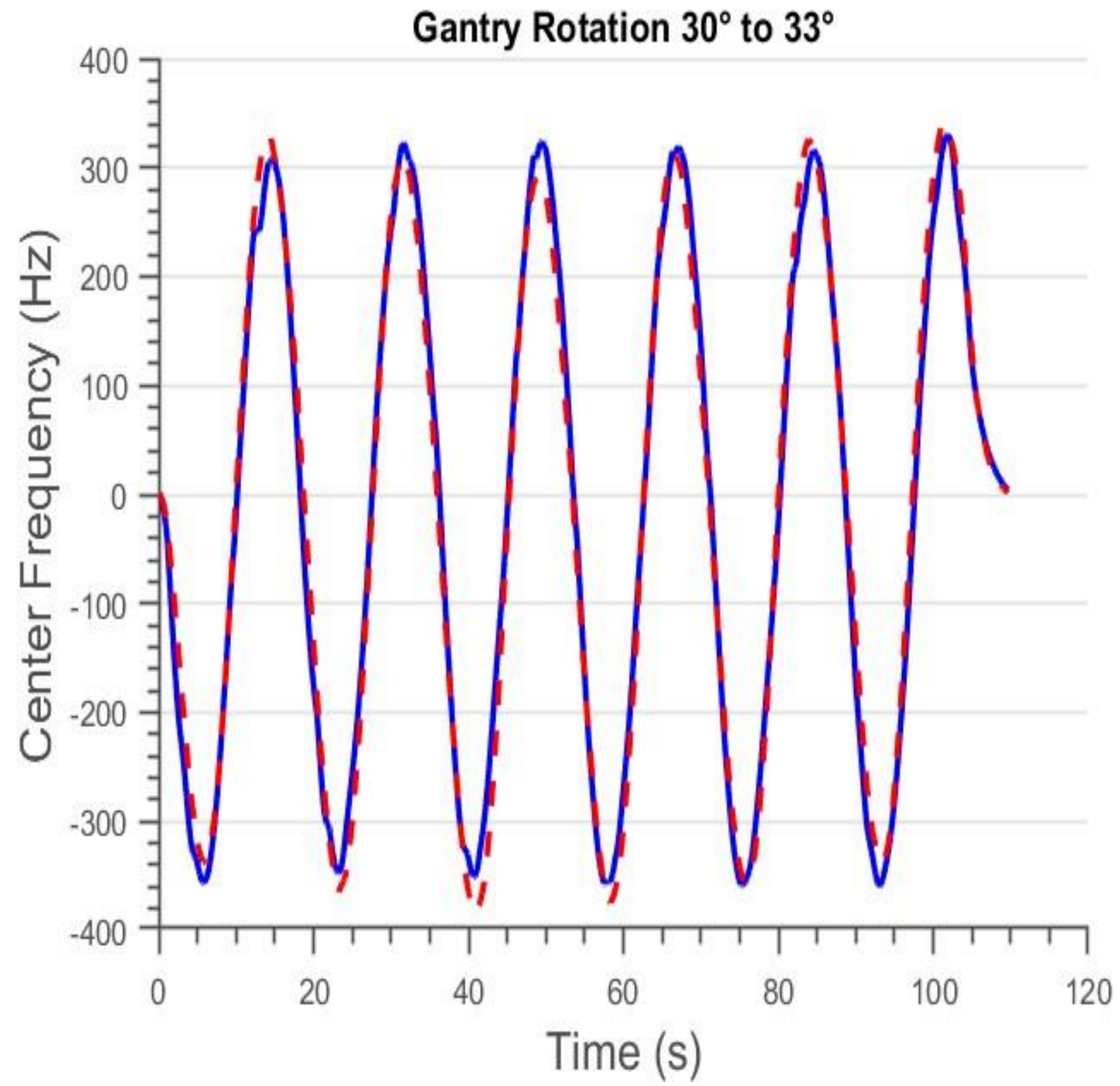

Figure 5.1: Model fit (red) compared to the measured B_0 fluctuation (blue) for a complete counterclockwise (30°→0°→270°→33°) rotation of the gantry. RMSE = 25.74 Hz

Similarly, the work done in **Chapter 4** could be expanded upon. Increasing the number of volunteers could improve the model's generalizability and overall performance. Additionally, integrating the artifact reduction model into an online reconstruction pipeline such as Gadgetron could be beneficial for real-time applicaitons.[84] The CycleGAN architecture utilized in **Chapter 4**, could be expanded or modified to incorporate k-space data. Model architectures that are designed to capture features in both k-space and the image domain may perform better than architectures that only rely on image domain data. The Resnet and U-Net architectures commonly used in CycleGAN generators are designed for data in the image domain and therefore cannot optimally extract features in k-space.[86] Additionally, other rapid imaging sequences could be utilized that are less susceptible to CIED artifacts (e.g. unbalanced steady state sequences, rapid gradient echo sequences) albeit with a tradeoff in temporal resolution, signal to noise ratios, and/or contrast to noise ratios.

References

1. Siegel RL, Miller KD, Fuchs HE, Jemal A. Cancer statistics, 2022. *CA Cancer J Clin*. 2022;72(1):7-33. doi:10.3322/caac.21708
2. National Cancer Institute. Radiation Therapy and You: Support for People With Cancer. *NCI Off Commun Public Liaison*. Published online 2016:54. www.cancer.gov/publications/patient-education
3. Baskar R, Lee KA, Yeo R, Yeoh KW. Cancer and radiation therapy: Current advances and future directions. *Int J Med Sci*. 2012;9(3):193-199. doi:10.7150/ijms.3635
4. Rammohan N, Randall JW, Yadav P. History of Technological Advancements towards MR-Linac: The Future of Image-Guided Radiotherapy. *J Clin Med*. 2022;11(16). doi:10.3390/jcm11164730
5. Ahunbay EE, Peng C, Chen GP, et al. An on-line replanning scheme for interfractional variations. *Med Phys*. 2008;35(8):3607-3615. doi:10.1118/1.2952443
6. Bertholet J, Knopf A, Eiben B, et al. Real-time intrafraction motion monitoring in external beam radiotherapy. *Phys Med Biol*. 2019;64(15). doi:10.1088/1361-6560/ab2ba8
7. Jaffray DA, Siewerdsen JH. Cone-beam computed tomography with a flat-panel imager: Initial performance characterization. *Med Phys*. 2000;27(6):1311-1323. doi:10.1118/1.599009
8. Otazo R, Lambin P, Pignol JP, et al. MRI-guided Radiation Therapy: An Emerging Paradigm in Adaptive Radiation Oncology. *Radiology*. 2021;298(2):248-260. doi:10.1148/RADIOL.2020202747
9. Mutic S, Dempsey JF. The ViewRay System: Magnetic Resonance-Guided and Controlled Radiotherapy. *Semin Radiat Oncol*. 2014;24(3):196-199. doi:10.1016/j.semradonc.2014.02.008
10. Green OL, Rankine LJ, Cai B, et al. First clinical implementation of real-time, real anatomy tracking and radiation beam control. *Med Phys*. 2018;45(8):3728-3740. doi:10.1002/mp.13002
11. Raaymakers BW, Jürgenliemk-Schulz IM, Bol GH, et al. First patients treated with a 1.5 T MRI-Linac: Clinical proof of concept of a high-precision, high-field MRI guided radiotherapy treatment. *Phys Med Biol*. 2017;62(23):L41-L50. doi:10.1088/1361-6560/aa9517

12. van Sörnsen de Koste JR, Palacios MA, Bruynzeel AME, Slotman BJ, Senan S, Lagerwaard FJ. MR-guided Gated Stereotactic Radiation Therapy Delivery for Lung, Adrenal, and Pancreatic Tumors: A Geometric Analysis. *Int J Radiat Oncol Biol Phys*. 2018;102(4):858-866. doi:10.1016/j.ijrobp.2018.05.048

13. Hoisak JDP, Sixel KE, Tirona R, Cheung PCF, Pignol JP. Correlation of lung tumor motion with external surrogate indicators of respiration. *Int J Radiat Oncol Biol Phys*. 2004;60(4):1298-1306. doi:10.1016/j.ijrobp.2004.07.681

14. Malinowski KT, McAvoy TJ, George R, Dieterich S, D'Souza WD. Mitigating errors in external respiratory surrogate-based models of tumor position. *Int J Radiat Oncol Biol Phys*. 2012;82(5):e709-e716. doi:10.1016/j.ijrobp.2011.05.042

15. Rudra S, Jiang N, Rosenberg SA, et al. Using adaptive magnetic resonance image-guided radiation therapy for treatment of inoperable pancreatic cancer. *Cancer Med*. 2019;8(5):2123-2132. doi:10.1002/cam4.2100

16. Henke L, Kashani R, Robinson C, et al. Phase I trial of stereotactic MR-guided online adaptive radiation therapy (SMART) for the treatment of oligometastatic or unresectable primary malignancies of the abdomen. *Radiother Oncol*. Published online 2017. doi:10.1016/j.radonc.2017.11.032

17. Klein EE, Hanley J, Bayouth J, et al. Task group 142 report: Quality assurance of medical acceleratorsa. *Med Phys*. 2009;36(9):4197-4212. doi:10.1118/1.3190392

18. Kim T, Gu B, Maraghechi B, et al. Characterizing MR Imaging isocenter variation in MRgRT. *Biomed Phys Eng Express*. 2020;6(3). doi:10.1088/2057-1976/ab7bc6

19. Cho I, Park JW, Cho B, et al. Dosimetric analysis of stereotactic rotational versus static intensity-modulated radiation therapy for pancreatic cancer. *Cancer/Radiothérapie*. 2018;22(8):754-762. doi:10.1016/J.CANRAD.2018.01.007

20. Kelly PJ, Mannarino E, Lewis JH, Baldini EH, Hacker FL. Total Dural Irradiation: RapidArc versus Static-Field IMRT: A Case Study. *Dosim*; 2012. doi:10.1016/j.meddos.2011.06.008

21. Oliver M, Ansbacher W, Beckham WA. Comparing Planning Time, Delivery Time and Plan Quality for IMRT, RapidArc and Tomotherapy. *J Appl Clin Med Phys. Phys*; 2009. doi: 10.1120/jacmp.v10i4.3068

22. Michael Gach H, Curcuru AN, Kim T, Yang D. Technical Note: Effects of rotating gantry on magnetic field and eddy currents in 0.35 T MRI-guided radiotherapy (MR-IGRT) system. *Med Phys*. 2021;48(11):7228-7235. doi:10.1002/mp.15226

23. Loo BW, Soltys SG, Wang L, et al. Stereotactic Ablative Radiotherapy for the Treatment of Refractory Cardiac Ventricular Arrhythmia. *Circ Arrhythmia Electrophysiol*. 2015;8(3):748-750. doi:10.1161/CIRCEP.115.002765

24. Cuculich PS, Schill MR, Kashani R, et al. Noninvasive Cardiac Radiation for Ablation of Ventricular Tachycardia. *New England Journal of Medicine* 377; 2017. doi:10.1056/NEJMoa1613773

25. Hidalgo-Tobon SS. Theory of gradient coil design methods for magnetic resonance imaging. *Concepts Magn Reson Part A*. 2010;36A(4):223-242. doi:https://doi.org/10.1002/cmr.a.20163

26. Liu H, Matson GB. Accurate measurement of magnetic resonance imaging gradient characteristics. *Materials (Basel)*. 2014;7(1):1-15. doi:10.3390/ma7010001

27. Tijssen RHN, Philippens MEP, Paulson ES, et al. MRI commissioning of 1.5T MR-linac systems – a multi-institutional study. *Radiother Oncol*. 2019;132:114-120. doi:10.1016/j.radonc.2018.12.011

28. Snyder JE, St-Aubin J, Yaddanapudi S, et al. Commissioning of a 1.5T Elekta Unity MR-linac: A single institution experience. *J Appl Clin Med Phys*. 2020;21(7):160-172. doi:10.1002/acm2.12902

29. Nejad-Davarani SP, Kim JP, Du D, Glide-Hurst C. Large field of view distortion assessment in a low-field MR-linac. *Med Phys*. 2019;46(5):2347-2355. doi:10.1002/mp.13467

30. Gach HM, Curcuru AN, Mutic S, Kim T. B0 field homogeneity recommendations, specifications, and measurement units for MRI in radiation therapy. *Med Phys*. 2020;47(9):4101-4114. doi:10.1002/mp.14306

31. Latifi K, Moros EG, Zhang G, Harrison L, Feygelman V. A Method to Determine the Coincidence of MRI-Guided Linac Radiation and Magnetic Isocenters. *Technol Cancer Res Treat*. 2019;18:1-6. doi:10.1177/1533033819877986

32. Bernstein MA, King K, Zhou X. *Handbook of MRI Pulse Sequences*. Elsevier; 2004. doi:10.1016/B978-0-12-092861-3.X5000-6

33. Ahn CB, Cho ZH. Analysis of the Eddy-Current Induced Artifacts and the Temporal Compensation in Nuclear Magnetic Resonance Imaging. *IEEE Trans Med Imaging*. 1991;10(1):47-52. doi:10.1109/42.75610

34. Nishimura DG. *Principles of Magnetic Resonance Imaging*. Stanford University; 2010.

35. Moussavi A, Untenberger M, Uecker M, Frahm J. *Correction of Gradient-Induced Phase Errors in Radial MRI*. Reson M, ed. 71; 2014.

36. Brodsky EK, Samsonov AA, Block WF. Characterizing and correcting gradient errors in non-Cartesian imaging: Are gradient errors Linear Time-Invariant (LTI)? *Magn Reson Med*. 2009;62(6):1466-1476. doi:10.1002/mrm.22100

37. Bieri O, Markl M, Scheffler K. *Analysis and Compensation of Eddy Currents in Balanced SSFP*. Vol 54. Reson M, ed. 2005;54:129-137; 2005. doi:10.1002/mrm.20527

38. Peshkovsky AS, Forguez J, Cerioni L, Pusiol DJ. RF probe recovery time reduction with a novel active ringing suppression circuit. *J Magn Reson*. 2005;177(1):67-73. doi:10.1016/J.JMR.2005.07.004

39. Robison RK, Li Z, Wang D, Ooi MB, Pipe JG. Correction of B 0 eddy current effects in spiral MRI. *Magn Reson Med*. 2019;81(4):2501-2513. doi:10.1002/mrm.27583

40. Bruijnen T, Stemkens B, van den Berg CAT, Tijssen RHN. Prospective GIRF-based RF phase cycling to reduce eddy current-induced steady-state disruption in bSSFP imaging. *Magn Reson Med*. 2020;84(1):115-127. doi:10.1002/mrm.28097

41. Michael Gach H, Curcuru AN, Wittland EJ, et al. MRI quality control for low-field MR-IGRT systems: Lessons learned. *J Appl Clin Med Phys*. 2019;20(10):53-66. doi:10.1002/acm2.12713

42. Duerst Y, Wilm BJ, Dietrich BE, et al. Real-time feedback for spatiotemporal field stabilization in MR systems. *Magn Reson Med*. 2015;73(2):884-893. doi:10.1002/mrm.25167

43. Jackson S, Glitzner M, Tijssen RHN, Raaymakers BW. MRI B0 Homogeneity and Geometric Distortion with Continuous Linac Gantry Rotation on an Elekta Unity *MR-Linac*. Phys. Med. Biol.. Biol; 2019.

44. Holt A, Van Gestel D, Arends MP, et al. Multi-institutional comparison of volumetric modulated arc therapy vs. intensity-modulated radiation therapy for head-and-neck cancer: a planning study. Published online 2013. doi:10.1186/1748-717X-8-26

45. Xhaferllari I, El-Sherif O, Gaede S. Comprehensive dosimetric planning comparison for early-stage, non-small cell lung cancer with SABR:fixed-beam IMRT versus VMAT versus TomoTherapy. *J Appl Clin Med Phys*. 2016;17(5):330. doi:10.1120/jacmp.v17i5.6291

46. Zhang K, Tian Y, Li M, Men K, Dai J. Performance of a multileaf collimator system for a 1.5T MR-linac. *Med Phys*. 2021;48(2):546-555. doi:10.1002/mp.14608

47. Michael Gach H, Curcuru AN, Kim T, Yang D. Technical Note: Effects of rotating gantry on magnetic field and eddy currents in 0.35 T MRI-guided radiotherapy (MR-IGRT) system. *Med Phys*. 2021;48(11):7228-7235. doi:10.1002/mp.15226

48. Bieri O, Scheffler K. Fundamentals of balanced steady state free precession MRI. *J Magn Reson Imaging*. 2013;38(1):2-11. doi:10.1002/jmri.24163

49. Waszak M, Falkovskiy P, Hilbert T, et al. Prospective head motion correction using FID-guided on-demand image navigators. *Magn Reson Med*. 2017;78(1):193-203. doi:10.1002/mrm.26364

50. Kober T, Marques JP, Gruetter R, Krueger G. Head motion detection using FID navigators. *Magn Reson Med*. 2011;66(1):135-143. doi:10.1002/mrm.22797

51. Benner T, van der Kouwe AJW, Kirsch JE, Sorensen AG. Real-time RF pulse adjustment for B0 drift correction. *Magn Reson Med*. 2006;56(1):204-209. doi:10.1002/mrm.20936

52. de Castro CSA, Boer VO, Luttje MP, et al. Temporal B0 Field Variation Effects on MRSI of the Human Prostate at 7T and Feasibility of Correction Using an Internal Field Probe. *NMR Biomed*. 2014;27:1353-1360

53. Boer VO, van de Bank BL, van Vliet G, Luijten PR, Klomp DWJ. Direct B0 field monitoring and real-time B0 field updating in the human breast at 7 Tesla. *Magn Reson Med*. 2012;67(2):586-591. doi:10.1002/mrm.23272

54. Deshpande VS, Shea SM, Li D. Artifact reduction in true-FISP imaging of the coronary arteries by adjusting imaging frequency. *Magn Reson Med*. 2003;49(5):803-809. doi:10.1002/mrm.10442

55. Chan TF, Vese LA. Active contours without edges. *IEEE Trans Image Process*. 2001;10(2):266-277. doi:10.1109/83.902291

56. Price R, Allison J, Clarke G, et al. Magnetic Resonance Imaging Quality Control Manual 2015. *Am Coll Radiol*. Published online 2015:120.

57. Zanche N De, Barmet C, Nordmeyer-Massner JA, Pruessmann KP. *NMR Probes for Measuring Magnetic Fields and Field Dynamics in MR Systems. Reson Med.* 2008;60:176-186

58. Dietrich BE, Brunner DO, Wilm BJ, et al. A Field Camera for MR Sequence Monitoring and System Analysis. *Reson Med*. 2016;75:1831-1840

59. Gross S, Barmet C, Dietrich BE, Brunner DO, Schmid T, Pruessmann KP. Dynamic Nuclear Magnetic Resonance Field Sensing with Part-per-Trillion Resolution. *Nat Commun*; 2016.

60. Gach HM, Curcuru AN, Wittland EJ, et al. MRI Quality Control for Low-Field MR-IGRT Systems: Lessons Learned. *J Appl Clin Med Phys*. Phys; 2019.

61. Eldeniz C, Fraum T, Salter A, et al. CAPTURE: Consistently Acquired Projections for Tuned and Robust Estimation: A Self-Navigated Respiratory Motion Correction Approach. *Invest. Radiol*; 2018.

62. Korin HW, Ehman RL, Riederer SJ, Felmlee JP, Grimm RC. Respiratory kinematics of the upper abdominal organs: a quantitative study. *Magn Reson Med*. 1992;23(1):172-178. doi:10.1002/mrm.1910230118

63. Kobayashi N, Parkinson B, Idiyatullin D, et al. Development and validation of 3D MP-SSFP to enable MRI in inhomogeneous magnetic fields. *Magn Reson Med*. 2021;85(2):831-844. doi:10.1002/mrm.28469

64. Mayinger M, Kovacs B, Tanadini-Lang S, et al. First magnetic resonance imaging-guided cardiac radioablation of sustained ventricular tachycardia. *Radiother Oncol J Eur Soc Ther Radiol Oncol*. 2020;152:203-207. doi:10.1016/j.radonc.2020.01.008

65. Gach HM, Green OL, Cuculich PS, et al. Lessons Learned From the First Human Low-Field MRI Guided Radiation Therapy of the Heart in the Presence of an Implantable Cardiac Defibrillator. *Pract Radiat Oncol*. 2019;9(4):274-279. doi:10.1016/j.prro.2019.02.003

66. Mesubi O, Ahmad G, Jeudy J, et al. Impact of ICD Artifact Burden on Late Gadolinium Enhancement Cardiac MR Imaging in Patients Undergoing Ventricular Tachycardia Ablation. *Pacing and Clinical Electrophysiology.* 37; 2014.

67. Liao H, Lin W-A, Zhou SK, Luo J. ADN: Artifact Disentanglement Network for Unsupervised Metal Artifact Reduction. Published online August 2, 2019. doi:10.1109/TMI.2019.2933425

68. Chen Y, Christodoulou AG, Zhou Z, Shi F, Xie Y, Li D. MRI Super-Resolution with GAN and 3D Multi-Level DenseNet: Smaller, Faster, and Better. 2020;(Debiao Li). http://arxiv.org/abs/2003.01217

69. Denck J, Guehring J, Maier A, Rothgang E. MR-contrast-aware image-to-image translations with generative adversarial networks. *Int J Comput Assist Radiol Surg*. 2021;16(12):2069-2078. doi:10.1007/S11548-021-02433-X/FIGURES/5

70. Wolterink JM, Leiner T, Viergever MA, Išgum I. Generative adversarial networks for noise reduction in low-dose CT. *IEEE Trans Med Imaging*. 2017;36(12):2536-2545. doi:10.1109/TMI.2017.2708987

71. Küstner T, Fuin N, Hammernik K, et al. CINENet: deep learning-based 3D cardiac CINE MRI reconstruction with multi-coil complex-valued 4D spatio-temporal convolutions. *Sci Rep*. 2020;10(1):1-13. doi:10.1038/s41598-020-70551-8

72. Choi H, Lee DS. Generation of structural MR images from amyloid PET: Application to MR-less quantification. *J Nucl Med*. 2018;59(7):1111-1117. doi:10.2967/jnumed.117.199414

73. Armanious K, Jiang C, Abdulatif S, Küstner T, Gatidis S, Yang B. Unsupervised medical image translation using Cycle-MeDGAN. *Eur Signal Process Conf*. 2019;2019-Septe. doi:10.23919/EUSIPCO.2019.8902799

74. Armanious K, Jiang C, Fischer M, et al. MedGAN: Medical image translation using GANs. *Comput Med Imaging Graph*. 2020;79:1-16. doi:10.1016/j.compmedimag.2019.101684

75. Yang G, Lv J, Chen Y, Huang J, Zhu J. Generative Adversarial Networks (GAN) Powered Fast Magnetic Resonance Imaging-Mini Review, Comparison and Perspectives. Published online 2021.

76. Zhu J, Park T, Efros AA, Ai B, Berkeley UC. Unpaired Image-to-Image Translation using Cycle-Consistent Adversarial Networks.

77. Liu Y, Lei Y, Wang T, Fu Y, Tang X. CBCT-based synthetic CT generation using deep-attention cycleGAN for pancreatic adaptive radiotherapy. Published online 2020:2472-2483. doi:10.1002/mp.14121

78. Du M, Liang K, Xing Y, Preparation AD. Reduction of metal artefacts in CT with Cycle-GAN. *2018 IEEE Nucl Sci Symp Med Imaging Conf Proc*. 2018;1:1-3.

79. Kida S. Visual enhancement of Cone-beam CT by use of CycleGAN. doi:10.1002/mp.13963

80. Nie D, Trullo R, Lian J, et al. Medical Image Synthesis with Deep Convolutional Adversarial Networks. *IEEE Trans Biomed Eng*. 2018;65(12):2720-2730. doi:10.1109/TBME.2018.2814538

81. Mao X, Li Q, Xie H, Lau RYK, Wang Z, Smolley SP. Least Squares Generative Adversarial Networks. *Proc IEEE Int Conf Comput Vis*. 2017;2017-Octob:2813-2821. doi:10.1109/ICCV.2017.304

82. He K. Deep Residual Learning for Image Recognition. arXiv:1512.03385 https://doi.org/10.48550/arXiv.1512.03385

83. Wang Z, Simoncelli EP, Bovik AC. Multiscale structural similarity for image quality assessment (Invited Paper). *The Thrity-Seventh Asilomar Conference on Signals, Systems & Computers,* 2003;2:9-13. doi: 10.1109/ACSSC.2003.1292216

84. Hansen MS, Sørensen TS. Gadgetron: an open source framework for medical image reconstruction. *Magn Reson Med*. 2013;69(6):1768-1776. doi:10.1002/mrm.24389

85. Vannesjo SJ, Haeberlin M, Kasper L, et al. Gradient system characterization by impulse response measurements with a dynamic field camera. *Magn Reson Med*. 2013;69(2):583-593. doi:10.1002/mrm.24263

86. Liu X, Pang Y, Jin R, Liu Y, Wang Z. Dual-domain reconstruction network with V-Net and K-Net for fast MRI. *Magn Reson Med*. 2022;88(6):2694-2708. doi:10.1002/mrm.29400